Thermal convection of viscoelastic fluids in concentric rotating cylinders: Elastic turbulence and kinetic energy budget analysis

A. Chauhan and C. Sasmal*

Department of Chemical Engineering, Indian Institute of Technology Ropar, Rupnagar, Punjab 140001, India

(Received 18 September 2023; accepted 20 May 2024; published 25 June 2024)

The introduction of solid polymers into a Newtonian solvent induces significant modifications in the flow behavior and heat transfer characteristics of resulting viscoelastic fluids. This study performs a comprehensive numerical investigation of thermal convection within a system comprising two concentric horizontal cylinders filled with viscoelastic fluids, with the inner cylinder rotating. The analysis encompasses all three modes of thermal convection, namely, forced, free, and mixed convection, over a range of Weissenberg numbers up to 20 and three values of the Richardson number, namely, 0, 1.429, and ∞, representing forced, mixed, and free convection modes of heat transfer, respectively. In forced convection, the flow field remains stable, while in free and mixed convection, an increase in the Weissenberg number leads to a transition from steady to unsteady periodic, quasiperiodic, and, finally, an aperiodic and chaotic behavior. This transition arises due to the presence of elastic instability and the subsequent appearance of elastic turbulence in viscoelastic fluids with the increasing Weissenberg number. Furthermore, our findings indicate that fluid viscoelasticity has minimal influence on heat transfer rates in the cases of forced and free convection. Conversely, heat transfer rates in mixed convection decrease initially with the Weissenberg number, and then it remains almost constant on further increasing its value. We conduct a detailed analysis of the viscoelastic kinetic energy budget to elucidate this deterioration in the heat transfer rate for viscoelastic fluids. We show that this diminished heat transfer results from kinetic energy transfer from the flow structure to polymer molecules, leading to decreased bulk motion within the system and, eventually, lesser heat transfer rates.

DOI: 10.1103/PhysRevFluids.9.063303

I. INTRODUCTION

Over the past several decades, the study of mixed convection heat transfer phenomena within a configuration comprising two horizontal concentric cylinders, known as a concentric annulus, has garnered substantial attention from the scientific community [1,2]. This system often involves the presence of one or both cylinders rotating, which adds an additional layer of complexity to the investigation. This particular configuration finds extensive practical and engineering applications, ranging from heat exchangers and nuclear reactors to thermal solar collectors and power generation systems. The fluid dynamics within this annular geometry become crucial in understanding the heat transfer processes involved [3–5]. The interaction between forced convection induced by the rotation of the inner cylinder and natural convection driven by temperature gradients leads to intriguing phenomena. As a result, numerous researchers have delved into this problem, conducting both experimental studies and numerical simulations to unravel the underlying mechanisms. The experiments provide valuable insights into the heat transfer characteristics, flow patterns, and thermal

*Contact author: csasmal@iitrpr.ac.in

performance, while numerical simulations offer a platform to explore the phenomena in a controlled and reproducible manner. Together, these studies have contributed to a deeper understanding of mixed convection heat transfer in the horizontal annulus with rotating inner cylinders, fostering advancements in diverse fields of application [6].

In the absence of cylinder rotation, heat transfer occurs solely due to natural convection in a concentric annulus. Extensive investigations of this geometry have been carried out using both experimental and numerical approaches. To name a few, for instance, Kuehn and Goldstein [7] conducted a detailed study with air and water, covering a wide range of Rayleigh numbers under steady flow conditions. They used the Mach-Zehnder interferometer technique for temperature evaluations and local heat transfer coefficient measurements, complemented by numerical investigations using the finite-difference method. Their results demonstrated excellent agreement between experimental and simulated temperature and velocity distributions at various positions within the annulus. Kumar [8] conducted a numerical study encompassing a broad range of Rayleigh numbers, from conduction- to convection-dominated steady flow states, while varying the diameter ratio between 1.2 and 10. Consistent with prior experiments, he observed crescent-shaped eddy patterns at small diameter ratios and kidney-shaped flow patterns at large diameter ratios. Yoo [9] performed numerical investigations to examine the impact of the Prandtl number on bifurcation phenomena and flow patterns within the annulus. This study revealed the existence of "upward flow" and "downward flow" depending on the value of the Prandtl number. Desai and Vafai [10] conducted a numerical investigation of turbulent natural convection inside a horizontal annulus across a wide range of Rayleigh and Prandtl numbers and radius ratios. They found a significant increase in heat transfer rate during the transition from laminar to turbulent flow, and this transition was delayed with increasing Prandtl numbers. Khanafer and Chamkha [11] studied the influence of a porous medium inside the annulus on natural convection heat transfer, while Nada and Said [12] investigated the effects of fins and their configurations on the same. A comprehensive review of the studies for this particular problem can be found in the literature [13,14], thereby contributing to a better understanding of this mode of heat transfer in the concentric annulus geometry.

On the other hand, numerous investigations have also focused on forced convective heat transfer within this concentric annulus geometry with a rotating cylinder, employing a combination of experimental and simulation approaches. Aoki *et al.* [15] conducted both theoretical and experimental studies on convective heat transfer in this configuration, specifically involving a rotating and heated inner cylinder. They identified a significant rise in the Nusselt number beyond a critical value of the Taylor number. Their theoretical predictions aligned well with experimental observations, and they proposed an empirical correlation for the Nusselt number. Lee [16] conducted numerical simulations, maintaining fixed values for the Prandtl number of 0.7 and radius ratio of 2.6 while varying the Rayleigh numbers and rotational speeds. The heat transfer rate increased with the Rayleigh number at any rotational speed but decreased with the rotational speed at a fixed Rayleigh number. In a subsequent study [17], Lee further explored the behavior at lower Prandtl numbers ranging from 0.01 to 0.1. At these low Prandtl numbers, the heat transfer rate from the inner rotating cylinder exhibited almost no dependence on the rotational speed or rotational Reynolds number. Gardiner and Sabersky [18] conducted experimental research, reaching high Taylor numbers of 10^6 and rotational Reynolds numbers of up to 7000. They observed a sudden increase in the heat transfer coefficient. For a comprehensive review of forced convective heat transfer in concentric annulus configurations with a rotating cylinder, Childs and Long [19] have presented an extensive overview of this topic.

The flow field and heat transfer phenomena in this concentric annulus geometry with a rotating cylinder become significantly more complex and intriguing when the buoyancy forces resulting from the temperature difference between the two cylinders are taken into account. Several studies have investigated this mixed convection heat transfer phenomenon in this particular system. For example, Fusegi *et al.* [20] conducted a numerical study spanning a range of Grashof numbers and mixed convection parameters (the ratio of Grashof and square of Reynolds numbers) between ∞ (indicating pure natural convection) and 1. They found that increasing the mixed convection

parameter led to higher heat transfer rates. Yoo [21] performed a numerical investigation on the concentric geometry with a cooled outer rotating cylinder, exploring a wide range of Rayleigh and Reynolds numbers for air with a Prandtl number of 0.7. They observed various flow patterns within the geometry, including one-eddy, two-eddy, and no-eddy configurations. Moreover, they noticed that the heat transfer rate decreased with the Reynolds number, regardless of the value of the Rayleigh number. Yang and Farouk [22] conducted a corresponding three-dimensional numerical study on mixed convection heat transfer in a concentric geometry with the inner rotating cylinder, varying the aspect ratios (the ratio of length to gap width between outer and inner cylinders). They found that the heat transfer rate reached an asymptotic value with the aspect ratio, independent of the mixed convection parameter. Kahveci [23] demonstrated that the flow field inside the annulus during mixed convection becomes unstable once the Rayleigh number surpasses a critical value. An increase in the Reynolds number and a decrease in the gap between the two cylinders facilitated this transition from stable to unstable flows.

The aforementioned literature indicates a considerable number of studies on forced or mixed convection heat transfer in concentric annulus geometry with a rotating cylinder. However, most of these studies focused on simple Newtonian fluids like air or water. In contrast, there is a significant lack of research on non-Newtonian fluids, particularly viscoelastic fluids. Many fluids, such as polymer melts, solutions, suspensions, and biofluids like blood, saliva, and synovial fluid, exhibit diverse non-Newtonian characteristics [24]. These fluids find extensive applications in various industries, including food, pharmaceuticals, cosmetics, and polymer processing, where they display both viscous and elastic behaviors, known as viscoelastic behavior [25,26]. Despite that, there is almost no study available for viscoelastic fluids in the literature. This is probably because of the presence of several challenges associated with viscoelastic fluid simulations. One of the main challenges in studying viscoelastic fluids numerically is the high-Weissenberg-number problem (HWNP), commonly encountered during simulations [27]. In this problem, the numerical solution diverges beyond a critical value of the Weissenberg number (denoted as $\mathrm{Wi} = \lambda\dot{\gamma}$, where λ is the fluid relaxation time, and $\dot{\gamma}$ is the strain rate) when dealing with flow through systems with geometric singularities. This divergence occurs due to the loss of positive definiteness in the stress tensor caused by steep gradients in variables like velocity and stress tensor. However, recent advancements, notably the log-conformation tensor approach introduced by Fattal and Kupferman [28], have made it possible to simulate significantly large values of the Weissenberg number without encountering the divergence problem.

In the flow of viscoelastic fluids, elastic instability often arises when the Weissenberg number exceeds a critical value. This instability is triggered by streamline curvature and normal elastic stresses [29,30]. As the Weissenberg number increases further, the flow state transits to elastic turbulence (ET), a more chaotic and turbulentlike flow state [31–33]. Research has shown that both elastic instability and elastic turbulence can significantly enhance heat transfer rates [34–38] and mixing efficiency [39–41], especially in microfluidic systems where steady and laminar flow conditions prevail [42]. In the context of mixed convection heat transfer, a recent study by Gupta *et al.* [43] revealed that the chaotic and fluctuating flow field resulting from elastic turbulence in viscoelastic fluids increased the heat transfer rate by more than 100% compared to simple Newtonian fluids in a lid-driven cavity. Furthermore, their subsequent study [44] investigated how the aspect ratio of the lid-driven cavity influenced the flow dynamics and heat transfer rate due to mixed convection. These findings highlight the potential of elastic instability and elastic turbulence in enhancing transport processes, particularly in microfluidic systems where steady and laminar flow conditions predominantly exist.

Some further research has also explored the impact of fluid viscoelasticity on heat transfer phenomena. For example, Cheng *et al.* [45] investigated the influence of fluid viscoelasticity on Rayleigh-Bénard convection (RBC) within a square cavity. Their findings revealed a nonmonotonic relationship between fluid viscoelasticity and heat transfer rates. Specifically, heat transfer rates initially decreased and then increased as the Weissenberg number increased. They conducted a turbulent kinetic energy (TKE) budget analysis to elucidate this trend. At low Weissenberg numbers,

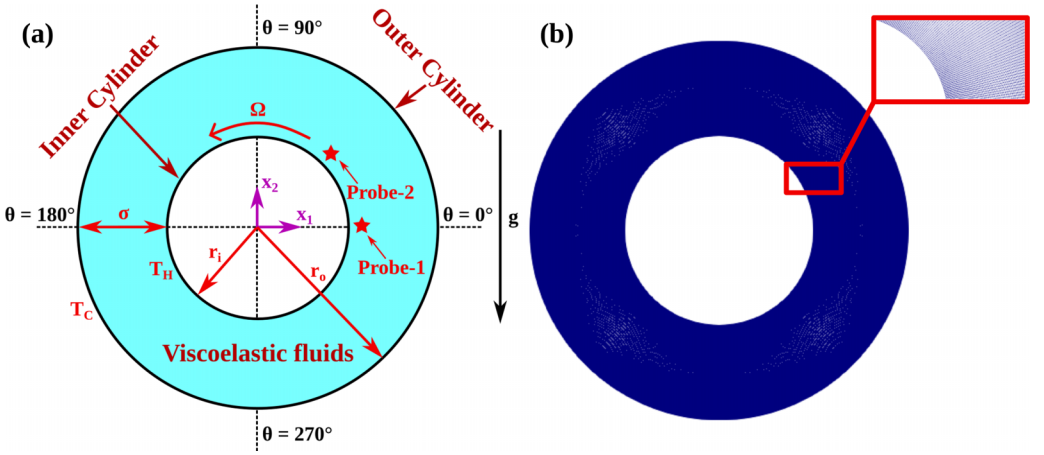

FIG. 1. (a) Schematic of the present problem and (b) the grid used in the present study. Note that the two probes, probe 1 and probe 2, within the annulus are located near the inner rotating cylinder at $(x_1, x_2) = (1.2, 0)$ and $(x_1, x_2) = (0.8, 0.8)$, respectively.

polymer additives acted as TKE sinks, leading to turbulent drag reduction (TDR) and heat transfer reduction (HTR). Conversely, at high Weissenberg numbers, polymer molecules acted as TKE sources, resulting in heat transfer enhancement (HTE). Other experimental [46] and numerical [47] studies also observed these HTR and HTE phenomena, while some studies only reported HTR [48]. Consequently, a debate persists regarding whether fluid viscoelasticity induced by polymer additives diminishes or enhances heat transfer rates. This ongoing debate underscores the significance of investigating convective heat transfer in viscoelastic fluids, motivating the present study.

In particular, this study aims to conduct a numerical investigation encompassing forced, free, and mixed convection heat transfer in viscoelastic fluids confined between two concentric horizontal cylinders, with the inner cylinder in rotation. Our investigation not only focuses on analyzing flow dynamics and heat transfer but also includes a detailed analysis of the viscoelastic kinetic energy budget to enhance our understanding of flow and heat transfer physics. We will employ the finite volume method based open-source code OPENFOAM [49] and RheoTool [50] to solve the governing equations, including mass, momentum, and energy equations, while considering the Oldroyd-B viscoelastic constitutive equation to mimic the rheological behavior of the present viscoelastic fluid. The rest of the paper is organized as follows: Section II provides problem details and governing equations, Sec. III outlines the numerical methodology, Sec. IV presents and discusses the results, and, finally, Sec. V summarizes the key findings of this study.

II. PROBLEM DESCRIPTION AND GOVERNING EQUATIONS

This study thoroughly explores thermal convection phenomena within a system consisting of two infinitely long horizontal concentric cylinders filled with viscoelastic fluids. The inner cylinder, with a radius of r_i, rotates at an angular velocity Ω, while the outer cylinder, with a radius of r_o, remains fixed, as illustrated in Fig. 1(a). This configuration leads to a ratio of inner cylinder diameter to annular gap width denoted as $\sigma_0 = \frac{2r_i}{r_o - r_i}$. The inner cylinder is kept at a higher temperature T_H compared to the temperature T_C of the outer cylinder ($T_H > T_C$). This temperature difference generates buoyancy-induced convection within the viscoelastic fluid kept between the two cylinders, while the rotating inner cylinder induces rotation-induced convection.

The present study examines all three modes of thermal convection: forced convection (rotation-induced convection only), free convection (buoyancy-induced convection only), and mixed convection (both buoyancy-induced and rotation-induced convection). In the presence of

buoyancy-induced thermal convection, the density variation is considered using the Boussinesq approximation: $\rho = \rho_{\text{ref}}[1 - \beta_T(T - T_{\text{ref}})]$, where ρ_{ref} is the reference density of the fluid at a reference temperature T_{ref}, and β_T represents the thermal volumetric expansion coefficient at constant pressure, defined as $\beta_T = -\frac{1}{\rho}\frac{\partial \rho}{\partial T}|_p$. In this study, the reference temperature is set as the temperature of the outer cylinder, i.e., $T_{\text{ref}} = T_C$. To maintain the validity of the Boussinesq approximation, a small temperature difference (<5 K) is applied between the inner and outer cylinder surfaces [51].

Additionally, it is assumed that the thermophysical properties of the viscoelastic fluid, such as specific heat capacity (C_p), thermal conductivity (k), polymer relaxation time (λ), and zero-shear rate viscosity (η_0), remain independent of temperature. The Oldroyd-B viscoelastic constitutive equation is used to represent the rheological behavior of the fluid [52], chosen for several reasons: (i) simplicity with only two parameters, polymer concentration and relaxation time; (ii) development based on the simplest polymer kinetic theory assuming a dumbbell-like polymer molecule with two beads connected by an infinitely stretchable elastic spring; and (iii) ability to accurately replicate the rheological behavior of constant shear viscosity viscoelastic fluids (or the so-called Boger fluids [53]), commonly employed for studying the explicit influence of fluid elasticity on flow dynamics and heat transfer. Under these assumptions, the governing equations in their dimensional forms are expressed as follows:
the continuity equation,

$$\frac{\partial u_i^*}{\partial x_i^*} = 0, \tag{1}$$

the momentum equation,

$$\rho\left(\frac{\partial u_i^*}{\partial t^*} + u_j^*\frac{\partial u_i^*}{\partial x_j^*}\right) = -\frac{\partial p^*}{\partial x_i^*} + \eta_s\frac{\partial}{\partial x_j^*}\left(\frac{\partial u_i^*}{\partial x_j^*}\right) + \frac{\partial \tau_{ij}^{p*}}{\partial x_j^*} + \rho g\beta_T(T - T_{\text{ref}})\delta_{i2}, \tag{2}$$

and the energy equation,

$$\rho C_p\left(\frac{\partial T}{\partial t^*} + u_j^*\frac{\partial T}{\partial x_j^*}\right) = k\frac{\partial}{\partial x_j^*}\left(\frac{\partial T}{\partial x_j^*}\right). \tag{3}$$

In the above equations, u_i^* is the velocity, x_i^* is the position, t^* is time, p^* is the pressure, η_s is the solvent viscosity, τ_{ij}^{p*} is the polymeric extra stress tensor, g is the acceleration due to gravity, T is the temperature, and δ_{ij} is the Kronecker delta. The polymeric extra stress tensor, τ_{ij}^{p*}, for an Oldroyd-B viscoelastic fluid model is evaluated using the following equation [52]:

$$\tau_{ij}^{p*} = \frac{\eta_p}{\lambda}(C_{ij} - \delta_{ij}), \tag{4}$$

$$C_{ij} + \lambda\overset{\nabla}{C}_{ij} = \delta_{ij}. \tag{5}$$

Here η_p is the polymeric viscosity, λ is the polymer relaxation time, C_{ij} is the polymeric conformation tensor, and $\overset{\nabla}{C}_{ij}$ is the upper-convected derivative of C_{ij}, which is given by the following equation:

$$\overset{\nabla}{C}_{ij} = \frac{\partial C_{ij}}{\partial t^*} + u_k^*\frac{\partial C_{ij}}{\partial x_k^*} - \frac{\partial u_i^*}{\partial x_k^*}C_{kj} - \frac{\partial u_j^*}{\partial x_k^*}C_{ik}. \tag{6}$$

Next, we nondimensionalize all these aforementioned governing equations using the following scaling variables:

$$x_i = \frac{x_i^*}{\sigma}, \quad u_i = \frac{u_i^*}{\Omega r_i}, \quad t = \frac{t^*\Omega r_i}{\sigma}, \quad p = \frac{p^*}{\rho_{\text{ref}}\Omega^2 {r_i}^2}, \quad \tau_{ij}^p = \frac{\tau_{ij}^{p*}\sigma}{\eta_p\Omega r_i}, \quad \text{and} \quad \phi = \frac{T - T_C}{T_H - T_C}.$$

The nondimensional forms of the above governing equations are written as below:

the continuity equation,

$$\frac{\partial u_i}{\partial x_i} = 0, \tag{7}$$

the momentum equation,

$$\frac{\partial u_i}{\partial t} + u_j \frac{\partial u_i}{\partial x_j} = -\frac{\partial p}{\partial x_i} + \frac{\beta}{\mathrm{Re}} \frac{\partial}{\partial x_j}\left(\frac{\partial u_i}{\partial x_j}\right) + \frac{1-\beta}{\mathrm{Re}} \frac{\partial \tau_{ij}^p}{\partial x_j} + \frac{\mathrm{Gr}}{\mathrm{Re}^2}\phi\delta_{i2}, \tag{8}$$

the energy equation,

$$\frac{\partial \phi}{\partial t} + u_j \frac{\partial \phi}{\partial x_j} = \frac{1}{\mathrm{RePr}} \frac{\partial}{\partial x_j}\left(\frac{\partial \phi}{\partial x_j}\right), \tag{9}$$

and the polymeric conformation tensor transport equation,

$$\frac{\partial C_{ij}}{\partial t} + u_k \frac{\partial C_{ij}}{\partial x_k} - \frac{\partial u_i}{\partial x_k} C_{kj} - \frac{\partial u_j}{\partial x_k} C_{ik} = \frac{\delta_{ij} - C_{ij}}{\mathrm{Wi}}. \tag{10}$$

In the above equations, $\mathrm{Re} = \frac{\rho \Omega r_i \sigma}{\eta_0}$ is the Reynolds number (ratio of the inertial to that of the viscous forces), $\mathrm{Pr} = \frac{C_p \eta_0}{k}$ is the Prandtl number (ratio of the momentum to that of the thermal diffusivity), $\mathrm{Gr} = \frac{\rho^2 g \beta_T (T_H - T_C) \sigma^3}{{\eta_0}^2}$ is the Grashof number (ratio of the buoyancy to that of the viscous forces), $\mathrm{Wi} = \frac{\lambda \Omega r_i}{\sigma}$ is the Weissenberg number (ratio of the elastic to that of the viscous forces), and $\beta = \frac{\eta_s}{\eta_0} = \frac{\eta_s}{\eta_s + \eta_p}$ is the polymer viscosity ratio (ratio of the solvent to that of the zero-shear rate viscosity of the polymer solution). As β approaches 1, the fluid demonstrates Newtonian behavior; conversely, it takes on the characteristics of a polymer melt as β approaches 0. In this study, we also employ another dimensionless parameter known as the Richardson number (Ri), defined as $\mathrm{Ri} = \frac{\mathrm{Gr}}{\mathrm{Re}^2}$. In general, when $\mathrm{Ri} < 0.1$, heat transfer is predominantly driven by forced convection. Conversely, for $\mathrm{Ri} > 10$, free convection dominates significantly. Mixed convection heat transfer occurs between these two limits, with a Richardson number ranging from 0.1 to 10. The above set of equations is valid for purely forced and mixed convection modes of heat transfer. In the limit of $\mathrm{Ri} \to 0$, the equations will reduce to that of purely forced convection heat transfer. However, in the case of purely free convection, a different set of equations will govern the flow field and heat transfer, presented in the Appendix. This is because the scaling variable for the velocity is different in this mode of heat transfer compared to that of forced and mixed convection due to the absence of cylinder rotation.

III. NUMERICAL METHODOLOGY

A. Simulation procedure

In this study, we have employed the finite volume method (FVM)-based open-source computational fluid dynamics (CFD) code OPENFOAM (version 7) [49] to solve all the governing equations, namely, mass, momentum, and energy equations. Additionally, we have utilized the recently developed *rheoHeatFoam* solver available in the RheoTool (version 5) package [50] to solve the Oldroyd-B viscoelastic constitutive equation. Among various discretization options, we have opted for the high-resolution CUBISTA scheme for discretizing advective terms in momentum, energy, and constitutive equations due to its improved iterative convergence properties [54]. We have utilized the second-order-accurate Gauss linear orthogonal interpolation scheme for diffusion terms in both momentum and energy equations. Gradient terms were discretized using the Gauss linear corrected scheme, and the Euler time-integration scheme was applied for time derivative terms. To solve the linear system of pressure fields, we have employed the preconditioned conjugate solver (PCG) with a DIC (diagonal-based incomplete Cholesky) preconditioner [55]. For solving velocity, temperature, and stress fields, the preconditioned biconjugate gradient solver (PBiCG) with a DILU (diagonal-based incomplete lower-upper) preconditioner was utilized [56]. The pressure-velocity

coupling was accomplished using the SIMPLE method. To enhance numerical stability, we have implemented the log-conformation tensor approach, initially introduced by Fattal and Kupferman [57] and later integrated into OPENFOAM by Pimenta and Alves [58]. Furthermore, we set a relative tolerance level of 10^{-8} for velocity, pressure, temperature, and stress fields.

B. Boundary and initial conditions

We have employed the following set of boundary and initial conditions for the numerical solution of the current problem.

Inner cylinder surface. An anticlockwise angular velocity of Ω is imposed. The temperature is kept constant at $\phi = 1$. The polymeric extra stresses are extrapolated linearly to the surface, and a zero-pressure gradient is applied.

Outer cylinder surface. The standard no-slip and no-penetration ($u_i = 0$) conditions for velocity are applied. Additionally, linear extrapolation is employed for polymeric extra stresses, and a zero-pressure gradient is maintained while the temperature is set to a fixed value of $\phi = 0$.

Furthermore, initial conditions involve all variables, including velocity vector, temperature, and polymeric extra stress tensor, being set to zero.

C. Grid and time independence studies

In addition to meticulous choices of discretization techniques, tolerance thresholds, and boundary conditions, it is imperative to select an optimal grid density that upholds result accuracy and precision in any computational fluid dynamics analysis. The time-step size is equally influential in problem resolution. In this study, we have followed the established procedure of employing the "blockMeshDict" subroutine in OPENFOAM to construct the computational domain and its meshing using regular cells. Ensuring stability and accuracy, we have maintained the Courant number ($\mathrm{Co} = \frac{u\Delta t}{\Delta x}$) below unity to satisfy the Courant-Friedrichs-Lewy (CFL) condition. Here, Δt represents the time-step size, and $\frac{\Delta x}{u}$ represents the characteristic convective timescale. We have observed $\mathrm{Co} \leqslant 0.3$ in all simulations when employing $\Delta t \leqslant 10^{-3}$. After identifying an appropriate time-step size for capturing temporal variations in fields like velocity, temperature, and stress, we have conducted a grid independence study. It is well established that as Reynolds and/or Grashof numbers increase, the hydrodynamic and/or thermal boundary layer thickness decreases, leading to steeper gradients near the inner and outer cylinder walls. To address this, grid refinement near these surfaces [as illustrated in Fig. 1(b)] becomes essential. Consequently, we have conducted a grid independence study at maximum Reynolds, Grashof, and Weissenberg numbers to capture steep gradients in thin boundary layers. For this study, we have considered Weissenberg numbers 5 and 20 to perform the grid independence study. The corresponding results on the time-averaged inner cylinder surface Nusselt number and the variation of the time-averaged velocity components at different azimuthal locations for different grid densities are presented in Table I and Fig. 2, respectively. After assessing these results, we have selected grid G2 with 60 480 cells for investigations up to $\mathrm{Wi} = 5$. Additionally, grid G3 with 120 000 cells proved sufficient for Weissenberg numbers ranging from 5 to 20. We have adopted two grids due to the transition to turbulentlike behavior as Weissenberg numbers exceeded 5. Increasing grid resolution in such conditions exacerbated fluctuations in velocity, temperature, stress, etc., making grid independence unattainable. An attempt to minimize error involved creating grid G4 with 240 000 cells, confirming convergence and reliability (within 2% of difference) of power spectral density (PSD) slopes for velocity and temperature fluctuations across grids G3 and G4 (results are not shown here). After the grid independence study, we performed the time independence study by selecting two time-step sizes. The corresponding results on the temporal fluctuation of the nondimensional velocity components and their power spectral density plots at two different probe locations are presented in Fig. 3. The results are found to be almost indistinguishable for the two time-step sizes chosen in the present work to carry out the time

TABLE I. Details of the grid independence study performed at Re = 100, Ra = GrPr = 10^5, and $\sigma_0 = 2$. Here, N_θ and N_r denote the number of cells on the surface of the inner cylinder and in the radial direction, respectively. The $\langle\cdot\rangle$ operator represents the time-averaged quantity.

Grid type	N_θ	N_r	Total cells	Time-step size	Wi = 5 $\langle Nu_{av}\rangle$	Wi = 20 $\langle Nu_{av}\rangle$
G1	300	100	30 000	1×10^{-3}	2.215	1.751
G2	432	140	60 400	1×10^{-3}	2.196	1.637
				5×10^{-4}	2.197	
G3	600	200	120 000	1×10^{-3}	2.195	1.584
				5×10^{-4}		1.581
G4	800	300	240 000	1×10^{-3}		1.545

independence study. Therefore, in summary, the results presented in this study are based on grid G2 for Wi $\leqslant$ 5 and grid G3 for 5 $<$ Wi $\leqslant$ 20 with a time-step size of $\Delta t = 10^{-3}$.

IV. RESULTS AND DISCUSSION

In this study, we have conducted comprehensive numerical simulations to investigate thermal convection phenomena in viscoelastic fluids confined between two concentric horizontal cylinders

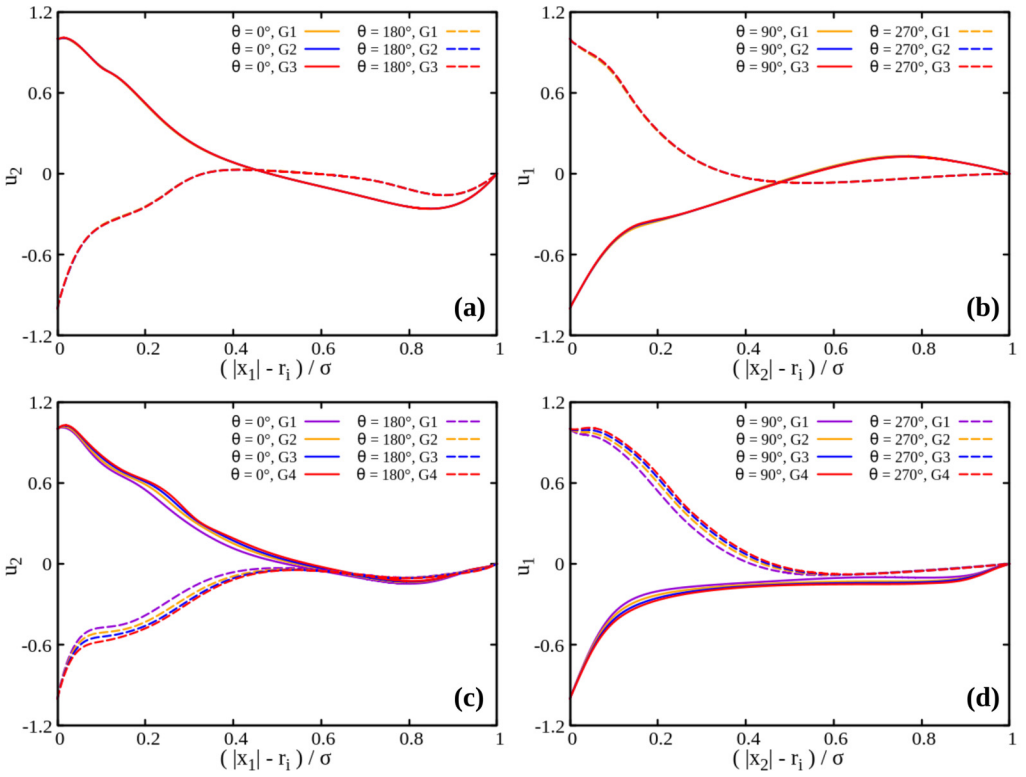

FIG. 2. Variation of the time-averaged nondimensional velocity components along the radial direction at different azimuthal locations for different grids considered in this study at [(a), (b)] Wi = 5 and [(c), (d)] Wi = 20.

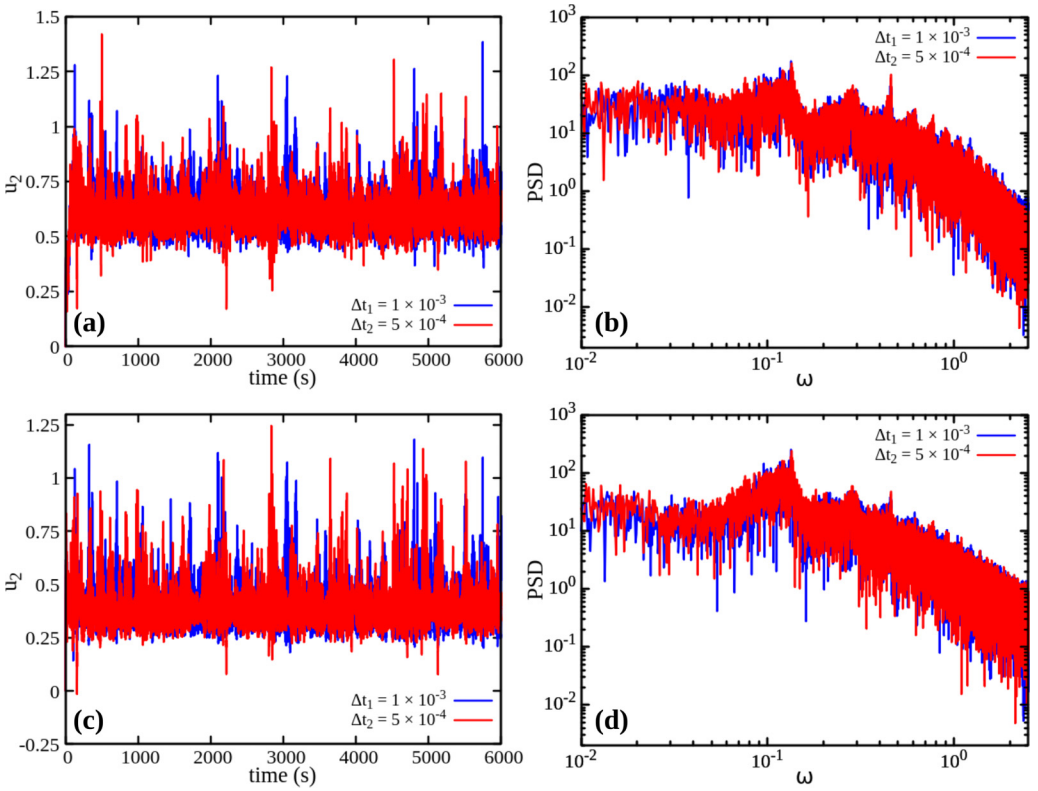

FIG. 3. Temporal variations of the nondimensional velocity component and the corresponding power spectral density plots of velocity fluctuations at two probe locations, [(a), (b)] probe 1 and [(c), (d)] probe 2 as shown in Fig. 1(a), near the inner cylinder surface for two different time-step sizes. Note that the grid used here is G3, and the Weissenberg number is kept fixed at Wi = 20.

with the inner one rotating. The parameters investigated included Reynolds number (Re = 100), Rayleigh number ($0 \leqslant \mathrm{Ra} \leqslant 10^5$), Weissenberg number ($0 \leqslant \mathrm{Wi} \leqslant 20$), polymer viscosity ratio ($\beta = 0.5$), Prandtl number (Pr = 7), and a fixed value of the ratio of inner cylinder diameter to annulus gap width ($\sigma_0 = 2$). The simulations covered forced, free, and mixed modes of heat transfer, facilitating a comprehensive comparative analysis of all three modes of heat transfer. The rheological behavior of the viscoelastic fluid was described using the Oldroyd-B constitutive equation, while the log-conformation tensor approach was employed to handle challenges related to the HWNP that often arises in viscoelastic fluid simulations. Additionally, simulations were carried out for a Newtonian fluid (Wi = 0 and $\beta = 1$) under identical conditions to investigate the impact of fluid viscoelasticity on flow dynamics and heat transfer. The obtained results were discussed in terms of streamlines and velocity magnitude, isotherms, averaged Nusselt number, and viscoelastic kinetic energy budget analysis. However, before presenting and discussing these new findings, we have ensured the accuracy and reliability of our present numerical tool by conducting validation studies against existing results that are available in the literature.

A. Code validation

First, we have verified the accuracy of our numerical code by comparing the results obtained with it against experimental and numerical results provided by Kuehn and Goldstein [7] for the pure

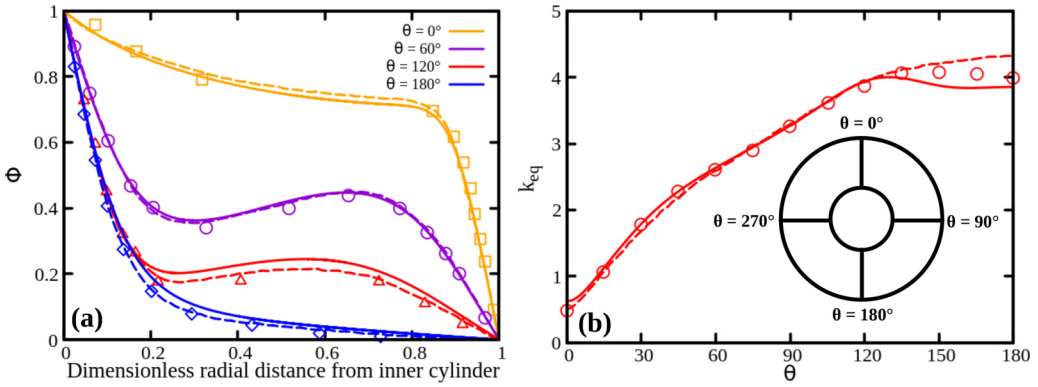

FIG. 4. Comparison of (a) the nondimensional temperature variation along the dimensionless radial distance from the inner cylinder and (b) the local equivalent thermal conductivity of the inner cylinder between the present results (solid lines) with that of experimental (symbols) and numerical results (dashed lines) of Kuehn and Goldstein [7] for the free convection case. The parameters used are Ra $= 5 \times 10^4$, Pr $= 0.7$, and $\sigma_0 = 1.25$.

free convection case between two horizontal concentric cylinders using air as the working fluid. The comparison, depicted in Fig. 4(a), illustrates the nondimensional temperature distribution variations along the dimensionless radial distance at various circumferential positions. Additionally, the local equivalent thermal conductivity of the inner cylinder along the circumferential direction is shown in Fig. 4(b). The agreement between our results and those of Kuehn and Goldstein [7] is acceptably close. Subsequently, we have validated our numerical tool for the mixed convection case within the same configuration of two horizontal concentric cylinders, using numerical outcomes provided by Yoo [21]. In Figs. 5(a) and 5(b), we have presented comparisons of the variation in local and average Nusselt numbers at different Reynolds numbers, maintaining a constant Rayleigh number of 5000. In both instances, a good concurrence is evident between our results and those presented by Yoo [21].

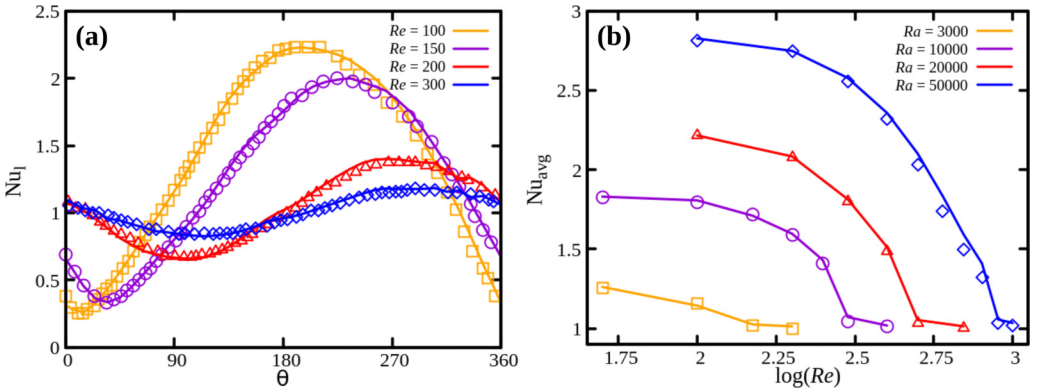

FIG. 5. Comparison of (a) the local Nusselt number along the surface of the inner cylinder at Ra $= 5000$ and (b) average Nusselt number between the present results (solid lines) with that of numerical results (symbols) of Yoo [21] for Pr $= 0.7$ and $\sigma_0 = 2$. In this case, the azimuthal coordinate θ was measured counterclockwise from the upward vertical through the center of the cylinders.

B. Flow dynamics

At the onset, we present an analysis of flow dynamics aspects within the current system encompassing all three modes of thermal convection: forced, mixed, and natural convection. Figure 6 depicts the nondimensional velocity magnitude and streamline patterns for different values of the Richardson (Ri) and Weissenberg (Wi) numbers. Notably, forced convection occurs when $\mathrm{Ri} = 0$ (first column in Fig. 6), while free convection becomes predominant as Ri approaches infinity (last column in Fig. 6). Meanwhile, mixed convection is characterized by an intermediate value of the Richardson number (middle column in Fig. 6). Moreover, the case with $\mathrm{Wi} = 0$ corresponds to that of a Newtonian fluid (first row in Fig. 6).

In the case of pure forced convection, irrespective of the value of the Weissenberg number, the streamlines follow the body contours of the cylinders. As a result, they appear to be concentric circles within the region between the two cylinders, irrespective of the value of the Weissenberg number. It mainly shows the existence of a solid-body-type rotation inside the system, where the relative distance between any two fluid parcels will remain the same all the time. The fluid velocity is solely in the circumferential direction, and there is no velocity in the radial direction. Therefore, one can expect no convective mixing of hot and cold fluids present near the hot inner and cold outer cylinders. Furthermore, the thickness of the hydrodynamic boundary layer and the velocity magnitude also remain the same regardless of the value of the Weissenberg number. All these suggest that the heat transfer will predominantly occur by the conduction mode, and its rate will be independent of the fluid type, i.e., Newtonian or viscoelastic. This will be discussed in detail in the subsequent section on heat transfer.

On the other hand, in the case of pure free convection, the fluid that is present at the bottom near the inner hot cylinder ($\theta = 270^\circ$) is heated up and becomes lighter so that it rises towards the top ($\theta = 90^\circ$). Therefore, it generates a buoyant plume that travels from the bottom region of the inner cylinder to the top region and forms a high-velocity magnitude zone in the middle of the upper gap region between the two cylinders. Ultimately, it touches the top region of the cold outer cylinder and travels down along the perimeter of the cylinder. Therefore, a buoyancy-induced circulation of hot and cold fluids is created inside the system. This leads to the mixing between them, and consequently one can expect a greater heat transfer rate than pure forced convection. Furthermore, due to this upward movement of the buoyant plume near the hot inner cylinder and downward movement near the cold outer cylinder, the streamlines are found to be highly distorted in this case as compared to circular ones seen in the pure forced convection case. In particular, two kidney-shaped recirculation regions are formed at the top region of the gap between the two cylinders. Moreover, the flow remains steady and symmetric along the vertical line passing through the origin of the present flow system for Newtonian fluids [Fig. 6(c)]. The fluid that is present at the bottom near the outer cold cylinder ($\theta = 270^\circ$) remains almost stagnant. On the other hand, for viscoelastic fluids with $\mathrm{Wi} = 5$ [Fig. 6(f)], the high-velocity magnitude zone is seen in the vicinity of both inner and outer cylinders in contrast to that seen at the top gap region between the two cylinders for Newtonian fluids. Two small vortices of equal size and shape appear at the bottom near the outer cylinder ($\theta = 270^\circ$), whose size increases as the Weissenberg number further increases to 10 [Fig. 6(i)]. However, those vortices disappear at a higher Weissenberg number of 20 [see Fig. 6(l)].

In the case of mixed convection, the flow dynamics within the system is governed by the interplay of buoyancy-driven and rotation-induced convection. Buoyancy-induced convection causes the fluid to move radially upward towards the upper gap region of the system, while rotation-induced convection pulls the fluid to rotate circumferentially. Consequently, these two convection mechanisms interact, with the strongest interaction occurring at the position $\theta = 90^\circ$ near the inner cylinder. The symmetry seen in the flow field along the vertical line drawn at the origin for free and forced convection modes of heat transfer is completely lost in this mixed convection mode of heat transfer. The kidney-shaped recirculation region formed in the left gap region between the two cylinders is completely destroyed. In contrast, the one formed in the right gap region increases in size and extends into the left gap region due to the rotation of the inner cylinder, as can be seen in Fig. 6(b)

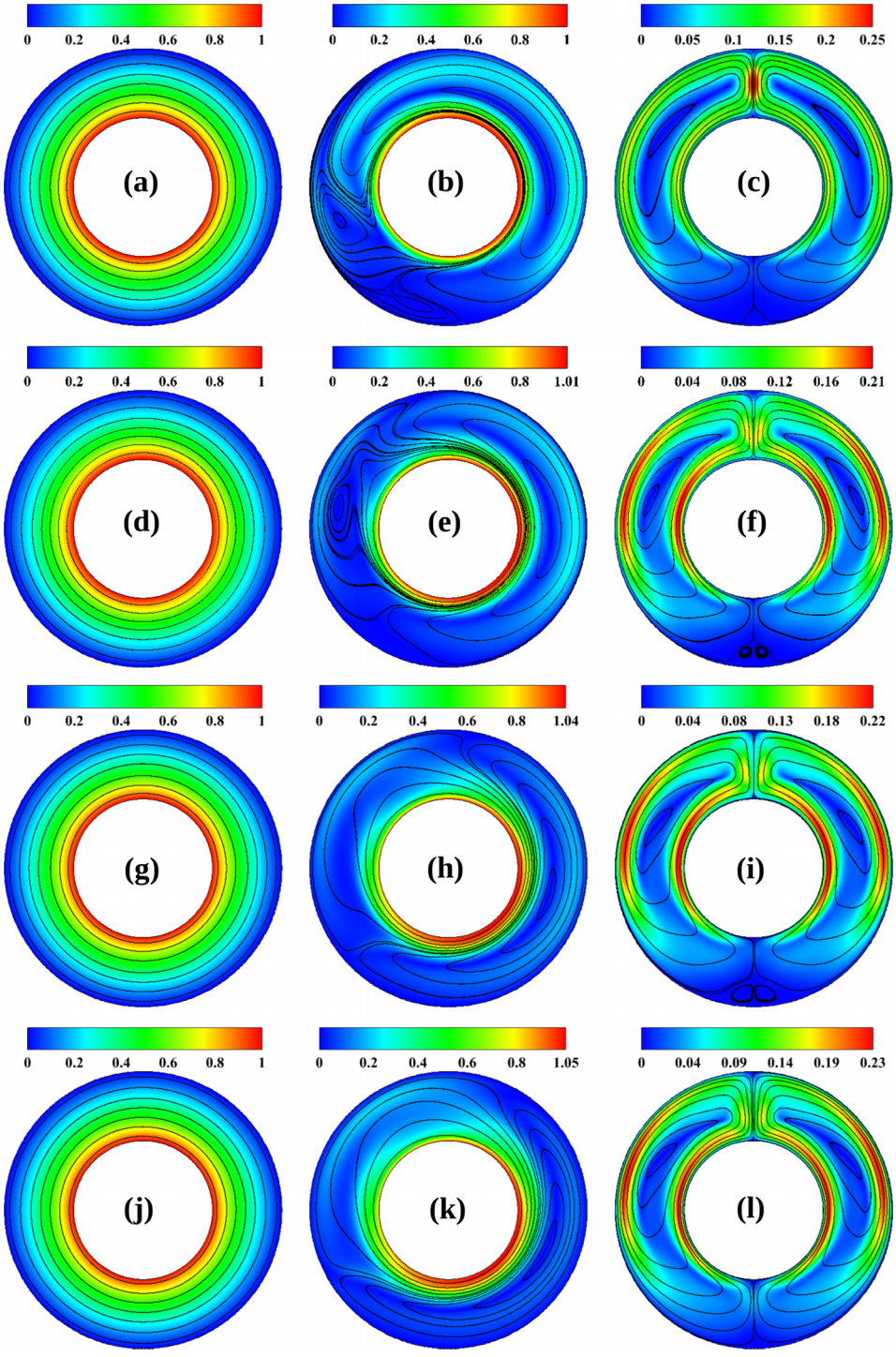

FIG. 6. Time-averaged nondimensional velocity magnitude contours and streamline patterns for different types of convection phenomena at (a) $\mathrm{Wi} = 0, \mathrm{Ri} = 0$; (b) $\mathrm{Wi} = 0, \mathrm{Ri} = 1.429$; (c) $\mathrm{Wi} = 0, \mathrm{Ri} \to \infty$; (d) $\mathrm{Wi} = 5, \mathrm{Ri} = 0$; (e) $\mathrm{Wi} = 5, \mathrm{Ri} = 1.429$; (f) $\mathrm{Wi} = 5, \mathrm{Ri} \to \infty$; (g) $\mathrm{Wi} = 10, \mathrm{Ri} = 0$; (h) $\mathrm{Wi} = 10, \mathrm{Ri} = 1.429$; (i) $\mathrm{Wi} = 10, \mathrm{Ri} \to \infty$; (j) $\mathrm{Wi} = 20, \mathrm{Ri} = 0$; (k) $\mathrm{Wi} = 20, \mathrm{Ri} = 1.429$; and (l) $\mathrm{Wi} = 20, \mathrm{Ri} \to \infty$.

for Newtonian fluids. The high-velocity magnitude zone is now seen in the region between $\theta = 0^\circ$ and 90°. The same trend is also seen for viscoelastic fluids. However, some stark differences are seen between the two fluids. For instance, the size of the kidney-shaped recirculation region is smaller for viscoelastic fluids than for Newtonian fluids, and it also extends to a lesser distance in the left gap region between the two cylinders [Fig. 6(e)]. The high-velocity magnitude zone is now shifted to the region between $\theta = 0^\circ$ and 270° in contrast to the region between $\theta = 0^\circ$ and 90° seen for Newtonian fluids. As the Weissenberg number and/or fluid elasticity gradually increases, the shifting of the high-velocity magnitude zone towards the region $\theta = 270^\circ$ is more noticeable. The thickness of this high-velocity magnitude zone increases, and the streamlines become more dispersed as the Weissenberg number increases, suggesting a gradual increase in the hydrodynamic boundary layer thickness with the Weissenberg number. For Newtonian fluids, a region of high-velocity magnitude zone (less than that formed near the inner cylinder) is also seen to form near the outer cylinder in the region between $\theta = 0^\circ$ and 270°. However, the magnitude of this region gradually decreases for viscoelastic fluids with the increasing values of the Weissenberg number. This suggests that the circulation of the hot and cold fluids inside the gap region between the two cylinders decreases as the Weissenberg number increases. This eventually tends to decrease the heat transfer rate from the inner hot cylinder, as it will be discussed in the subsequent section. Furthermore, the kidney-shaped recirculation region in the right gap region between the two cylinders gradually shifts towards the bottom region as the Weissenberg number gradually increases. Interestingly, the distortion in the streamlines decreases as the Weissenberg number increases; for instance, see the streamline patterns presented for Weissenberg numbers 5 and 20 in Figs. 6(e) and 6(k), respectively. Therefore, a significant difference in flow dynamics emerges within the present system depending upon the type of heat transfer mode and the Weissenberg number. This difference, in turn, substantially influences the ensuing heat transfer characteristics, an aspect that will be discussed in the subsequent section.

Note that the results on streamlines and velocity magnitude are obtained here based on time-averaged velocity fields. Therefore, it cannot predict the temporal nature of the flow field, i.e., whether it is steady or unsteady. However, one would expect a flow transition from steady to unsteady in the present system, particularly for viscoelastic fluids, due to the presence of elastic instability and the subsequent elastic turbulence caused by the interaction between the normal elastic stresses and the streamline curvature of the present geometry [30,32,33]. The fluctuation in the flow field arising due to this flow transition is demonstrated in Fig. 7 wherein the time-averaged root mean square velocity magnitude fluctuation is presented for all three modes of heat transfer cases. It is defined as $(u_{\mathrm{rms,mag}} = \sqrt{\langle(\tilde{u}_{\mathrm{mag}} - \bar{u}_{\mathrm{mag}})^2\rangle_t})$ where $\tilde{u}_{\mathrm{mag}}$ is the instantaneous velocity magnitude whereas $\bar{u}_{\mathrm{mag}}$ is its time-averaged value. Irrespective of the heat transfer mode, it can be clearly seen that the fluctuation in the flow field increases with the Weissenberg number due to the increase in the intensity of elastic instabilities. In the case of mixed convection, the fluctuation is seen to be more noticeable near the inner cylinder region between $\theta = 0^\circ$ and 90° where the interaction between the rotation-induced and buoyancy-induced convection is more intense [Figs. 7(b) and 7(c)]. In contrast, the fluctuation is seen to be more in the upper gap region between the two cylinders at $\theta = 90^\circ$ in the case of free convection. However, the magnitude of velocity fluctuation is found to be higher in mixed convection compared to free or forced convection, regardless of the value of the Weissenberg number.

To further characterize the nature of this fluctuating flow field under various heat transfer modes and different Weissenberg number values, Fig. 8 illustrates the temporal evolution of the nondimensional u_2 velocity component at a specific probe location near the inner cylinder [probe 1 in Fig. 1(a)] and its corresponding PSD plot. In the case of forced convection (Ri = 0), as depicted in Fig. 8(a), the velocity component remains constant over time up to Weissenberg number 10, suggesting the presence of a steady flow field. However, at Wi = 20, it fluctuates with time, which signifies the transition of the flow field from steady to unsteady at this Weissenberg number. The fluctuation is quasiperiodic in nature, which is governed by a single dominant frequency along with some secondary frequencies, as can be evident from the PSD plot presented in Fig. 8(b). In the case of mixed convection, the velocity component starts to fluctuate even at a lesser Weissenberg number

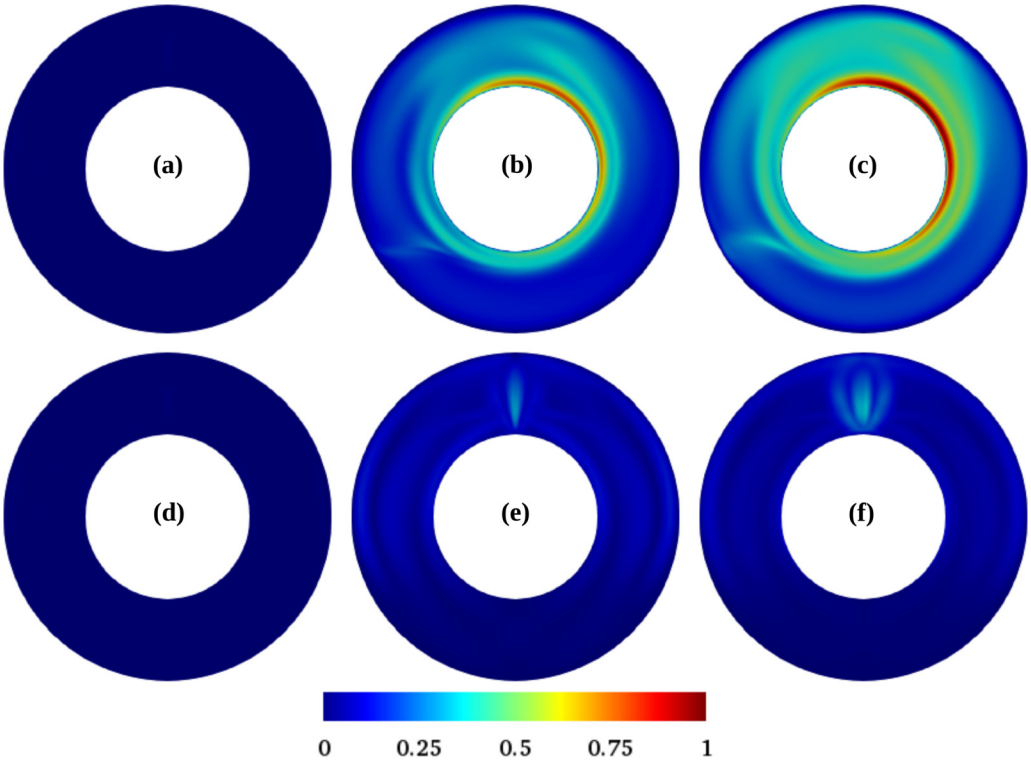

FIG. 7. Variation of the root mean square velocity magnitude fluctuations for different values of the Weissenberg number and Richardson number, namely, (a) Wi = 0, Ri = 1.429; (b) Wi = 14, Ri = 1.429; (c) Wi = 20, Ri = 1.429; (d) Wi = 0, Ri $\to \infty$; (e) Wi = 14, Ri $\to \infty$; and (f) Wi = 20, Ri $\to \infty$. Here, the root mean square velocity magnitude is presented on a scale of 0 to 1 after rescaling with its maximum value obtained at Wi = 20, Ri = 1.429.

of 5 [Fig. 8(c)], indicating an early transition of the flow field from steady to unsteady for this mode of heat transfer wherein the fluctuation is seen to be quasiperiodic in nature [Fig. 8(d)]. As the Weissenberg number further increases to higher values, the flow field transits from a quasiperiodic to a more chaotic state. In the corresponding PSD plot, the presence of several dominant as well as secondary frequencies across a wide range of values indicates the presence of an elastic turbulence phenomenon within the present geometry at higher Weissenberg numbers in this mode of heat transfer. This trend in the PSD plot reveals the excitation of fluid motion across a broad range of continuum frequencies, which is characteristic of elastic turbulence in flows of viscoelastic fluids. In the low-frequency range, a plateau is observed in the power spectrum, while at high frequencies, a power-law decay (ω^{α}) is evident, covering almost two orders of magnitude in the frequency range. The fitted value of the power-law exponent α is -4.37, and the same range of values was obtained experimentally for various geometries, thereby confirming the presence of elastic turbulence [31–33]. In the case of free convection, the flow field exhibits unsteadiness at a Weissenberg number of 8 [Fig. 8(e)]. It is seen to be periodic in nature, as highlighted by the presence of a single dominant frequency peak in the PSD plot presented in Fig. 8(f). With the further gradual increment of the Weissenberg number, the flow progressively transits to a quasiperiodic and then to a chaotic turbulentlike state, likewise seen in the mixed convection mode of heat transfer.

Therefore, irrespective of the heat transfer mode, a gradual transition in the flow field happens from steady to unsteady periodic to unsteady quasiperiodic and finally to a more chaotic aperiodic state as the Weissenberg number gradually increases in the case of viscoelastic fluids in comparison

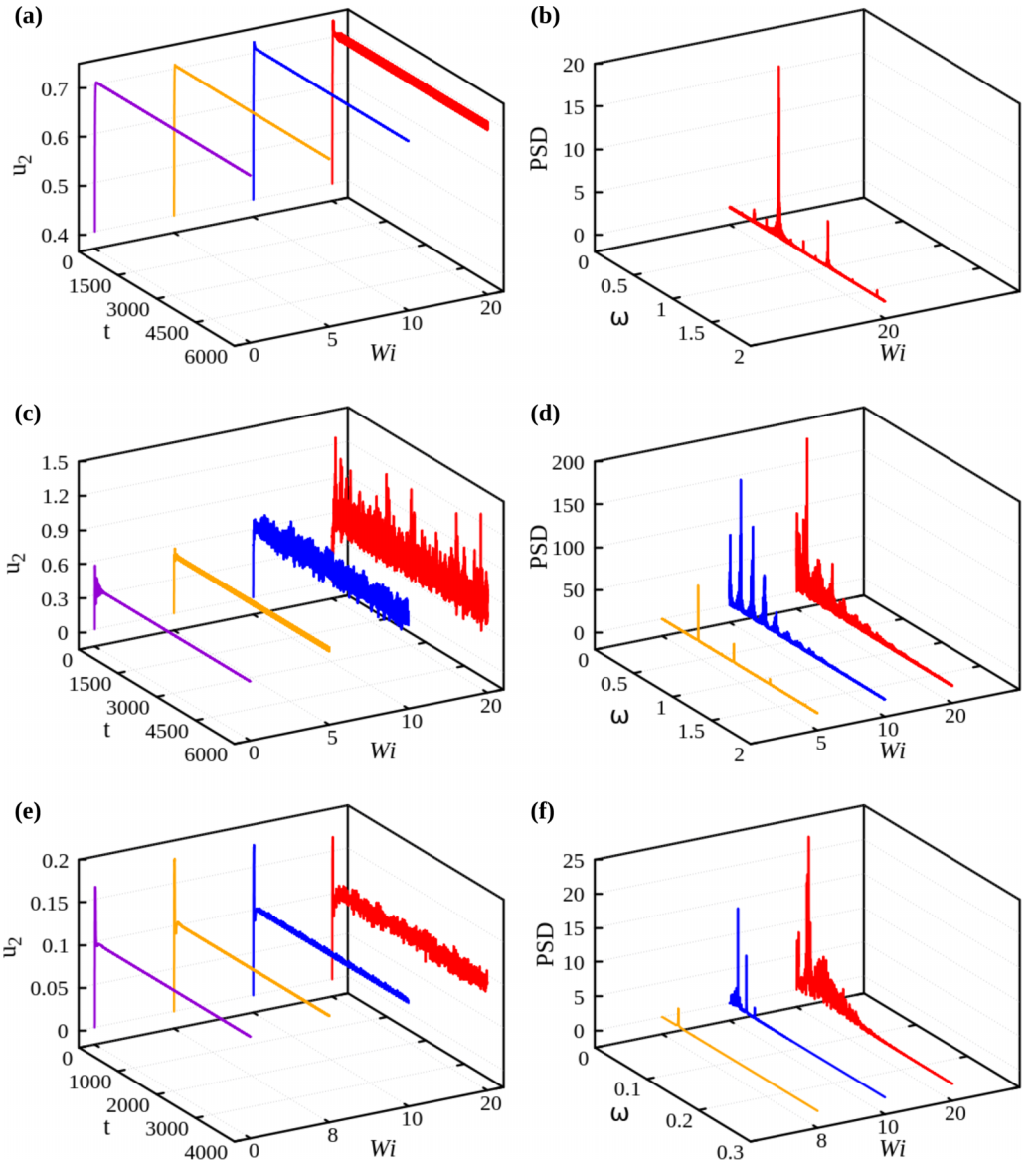

FIG. 8. Temporal variation of the nondimensional velocity component at a probe location near the inner cylinder surface ($x_1 = 1.2, x_2 = 0$) for (a) Ri $= 0$, (c) Ri $= 1.429$, and (e) Ri $\to \infty$. The corresponding power spectral density curves represent (b) Ri $= 0$, (d) Ri $= 1.429$, and (f) Ri $\to \infty$.

to a steady flow state for the Newtonian fluids. This transition occurs due to the occurrence of elastic instability in flows of viscoelastic fluids, which, as mentioned earlier, originates due to the interaction between the streamline curvature and normal elastic stresses present in a viscoelastic fluid [30]. The magnitude of elastic polymeric stresses increases with the Weissenberg number, as shown in Fig. 9. It can be seen that the magnitude of polymeric stress is mostly higher in the vicinity of the inner cylinder, where severe stretching of polymer molecules happens due to its rotation. However, in the case of free convection, a high-magnitude stress zone is also observed near the outer cylinder due to the downward motion of the fluid in this region. Furthermore, the polymeric

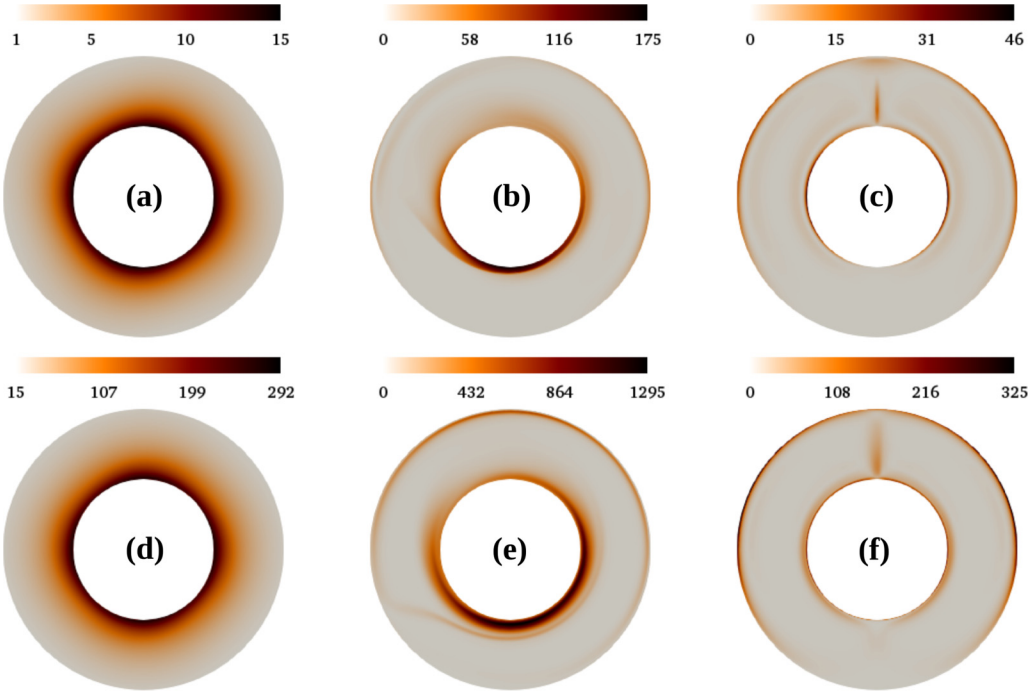

FIG. 9. Variation of the time-averaged magnitude of polymeric extra stress tensor ($|\tau_{ij}^{p}|$) for different values of Weissenberg and Richardson numbers, namely, (a) Wi = 1, Ri = 0; (b) Wi = 1, Ri = 1.429; (c) Wi = 1, Ri $\to \infty$; (d) Wi = 20, Ri = 0; (e) Wi = 20, Ri = 1.429; and (f) Wi = 20, Ri $\to \infty$.

stress is much higher for the mixed convection case than for the cases of forced and free convection. Therefore, one would expect a much higher intensity in the elastic instability and subsequent elastic turbulence phenomena in the mixed convection case of heat transfer of viscoelastic fluids, which was also evident in the analysis of temporal velocity fluctuation at a probe location presented in Fig. 8 and variation in the time-averaged root mean square velocity magnitude fluctuation shown in Fig. 7. Furthermore, polymeric stresses are seen to be gradually concentrated near the cylinders as the Richardson number gradually increases. This is because as the value of Ri increases, the buoyancy-induced convection increases, whereas the rotation-induced convection decreases. The former results in a narrow high-velocity magnitude zone in the vicinity of the cylinders, whereas the latter causes the velocity field to be gradually dispersed due to the presence of a solid-body type rotation, as can be seen from Fig. 6. This ultimately causes the polymer molecules to be highly stretched (and hence high polymeric stresses) in the proximity of cylinders with high Ri values.

C. Heat transfer

Having explored the flow dynamics, we now delve into the heat transfer characteristics within the current system, focusing on the same combinations of Richardson and Weissenberg numbers as depicted in Fig. 6 for the flow dynamics. Figure 10 provides a surface plot depicting the nondimensional temperature distribution and isotherms for various Richardson and Weissenberg number values. In the context of pure forced convection (Ri = 0), as presented in the first column of Fig. 10, the isotherms exhibit a pattern akin to concentric circles, resembling the streamlines observed in the flow field. Here, there is a gradual temperature diffusion from the hot inner cylinder towards the outer cylinder, independent of the Weissenberg number's value. It occurs due to the

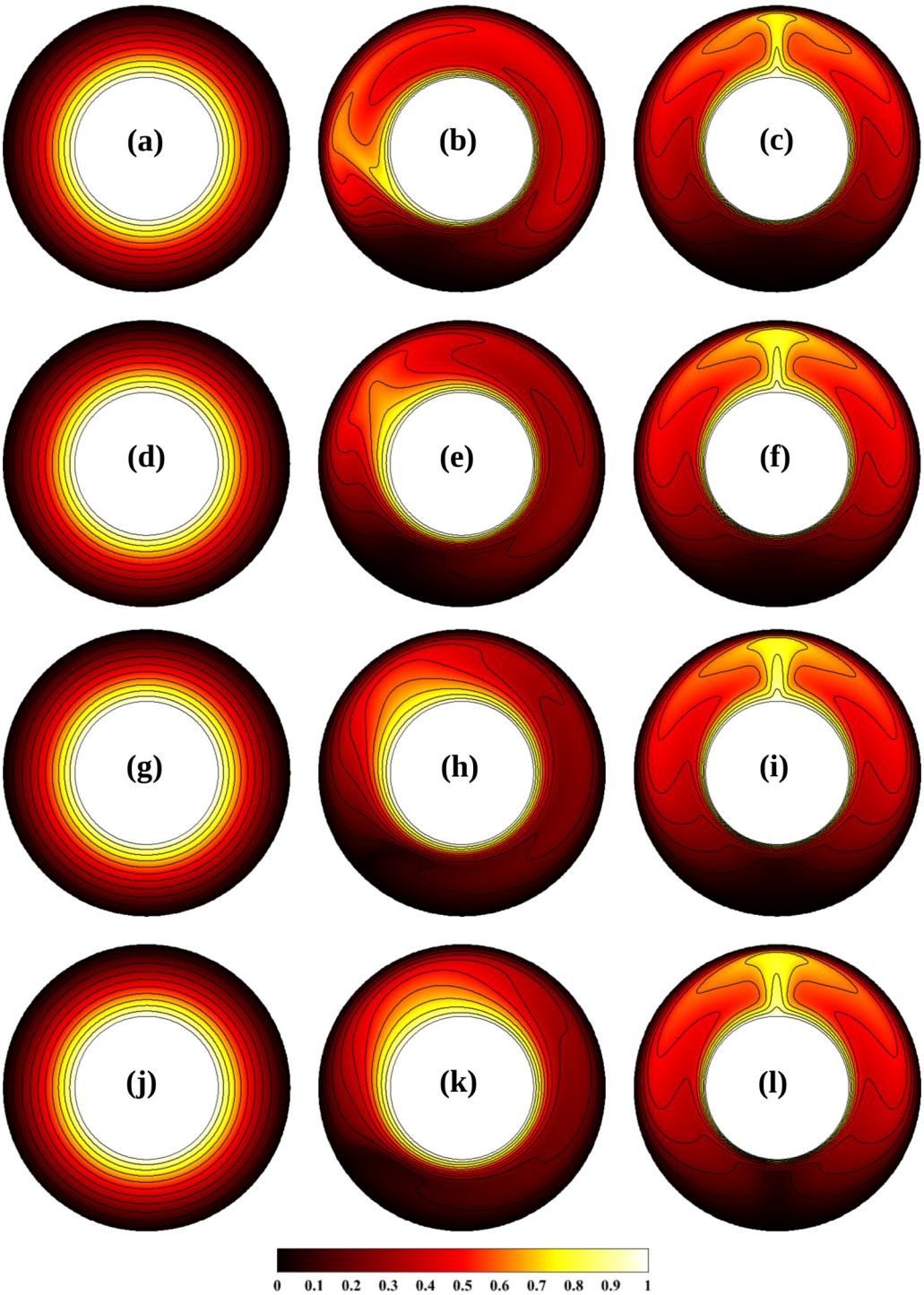

FIG. 10. Time-averaged surface plot of temperature distribution and isotherm contours for various types of convection phenomena at (a) Wi = 0, Ri = 0; (b) Wi = 0, Ri = 1.429; (c) Wi = 0, Ri → ∞; (d) Wi = 5, Ri = 0; (e) Wi = 5, Ri = 1.429; (f) Wi = 5, Ri → ∞; (g) Wi = 10, Ri = 0; (h) Wi = 10, Ri = 1.429; (i) Wi = 10, Ri → ∞; (j) Wi = 20, Ri = 0; (k) Wi = 20, Ri = 1.429; and (l) Wi = 20, Ri → ∞.

presence of solid-body-like rotation within the current flow system, implying that heat transfer primarily will occur through conduction in this case.

On the other hand, in the case of pure free convection (with $\mathrm{Ri} \to \infty$), as depicted in the last column of Fig. 10, the isotherms exhibit more pronounced distortion compared to the case of pure forced convection. This distortion arises due to the fluid's recirculation along the perimeter of the hot inner cylinder towards the outer cold cylinder. The isotherms are notably concentrated in the vicinity of the hot inner cylinder, indicating the presence of a thin thermal boundary layer in this region. At the top gap region, located at $\theta = 90^\circ$ between the two cylinders [Fig. 10(c)], the isotherms adopt a mushroomlike shape. As the Weissenberg number increases, the size of this mushroomlike shape seems to increase. However, the overall isotherm pattern remains almost the same. This suggests that the fluid elasticity for this mode of heat transfer will hardly influence the heat transfer rate. The temperature of the fluid near the region $\theta = 270^\circ$ remains almost constant to a value of zero, exhibiting reduced mixing of hot and cold fluids in this region and thereby suggesting the lowest heat transfer rate in this region. This is because the fluid in this region remains almost stagnant, as was also evident from the streamlines and velocity magnitude plots presented in Fig. 6.

In contrast, during mixed convection heat transfer, the isotherms near the inner hot cylinder adopt a circular shape akin to the cylinder itself. However, as we move away from the inner cylinder, the isotherms exhibit distortion, which is particularly pronounced for Newtonian fluids [Fig. 10(b)]. As the Weissenberg number gradually increases, this distortion in the isotherms away from the inner cylinder diminishes, and those isotherms also become almost concentric in nature; for instance, see Fig. 10(k) for the results at $\mathrm{Wi} = 20$. Furthermore, it is worth noting that the isotherms become increasingly dispersed in the vicinity of the inner hot cylinder, indicating a gradual increase in the thermal boundary layer thickness as the Weissenberg number increases. Consequently, one would anticipate a deterioration in the heat transfer rate with an increase in the Weissenberg number during mixed convection. This effect will now be quantitatively examined through the variation of the Nusselt number, calculated along the surface of the hot inner cylinder. The local value of this Nusselt number, denoted as (Nu_l), at a point on the inner cylinder's surface is estimated as follows:

$$\mathrm{Nu}_l = \frac{h_l \sigma}{k} = -\left(\frac{\partial \phi}{\partial \boldsymbol{n}_s}\right)_{\text{surface}}, \tag{11}$$

where h_l is the local heat transfer coefficient and $\boldsymbol{n}_s$ is the unit normal vector drawn on the surface of the inner cylinder. Furthermore, the surface average values ($\mathrm{Nu}_{\mathrm{av}}$) of this local Nusselt number are obtained by integrating the local values over the whole surface of the inner cylinder as follows:

$$\mathrm{Nu}_{\mathrm{av}} = \frac{h\sigma}{k} = \frac{1}{S}\int_S \mathrm{Nu}_l \, dS, \tag{12}$$

where h is the average heat transfer coefficient. Figure 11 illustrates how the time-averaged values of the surface-averaged Nusselt number ($\langle \mathrm{Nu}_{\mathrm{av}} \rangle$) vary with the Weissenberg number at different Richardson number values. Notably, during forced convective heat transfer, $\langle \mathrm{Nu}_{\mathrm{av}} \rangle$ remains nearly constant at around 1 across the entire range of Weissenberg numbers investigated in this study. This value of the average Nusselt number suggests that heat transfer predominantly occurs via conduction in this case, with limited dependence on the fluid's kinematic properties, such as viscosity and relaxation time. Therefore, the heat transfer rate remains consistent and is not dependent upon the Weissenberg number.

In contrast, in the case of pure free convection ($\mathrm{Ri} \to \infty$), the heat transfer rate increases due to the presence of buoyancy-induced convection within the system. This convection facilitates mixing hot fluid near the inner cylinder with cold fluid near the outer cylinder, enhancing heat transfer. As a result, the average Nusselt number increases by approximately three times compared to forced convection. However, once again, the Nusselt number values show minimal dependence on the Weissenberg number in this mode of heat transfer. This is likely because, while buoyancy-induced convection currents are generated in this mode, their strength is comparatively lower than that observed in forced or mixed convection. This is evident in Fig. 6, which presents the velocity

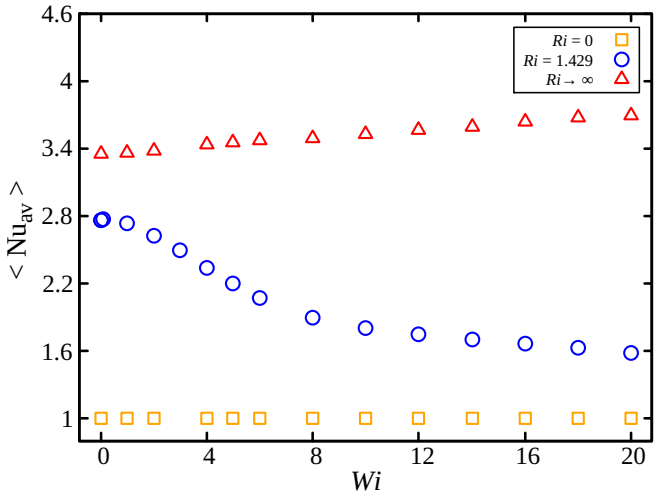

FIG. 11. Variation of the surface- and time-averaged Nusselt number calculated on the surface of the inner cylinder with Weissenberg number for all three modes of heat transfer, namely, forced (Ri = 0), mixed (Ri = 1.429), and natural (Ri → ∞) convection.

magnitude for different heat transfer modes. This lower strength of buoyancy-induced convection currents results in less stretching of polymer molecules and generates lesser elastic stresses, which are insufficient to transit the flow field into the regime of a chaotic flow state, where a significant change in heat transfer rate with the Weissenberg number would be expected.

On the other hand, in the mixed convection case, a different trend is observed in the variation of the average Nusselt number. In this mode of heat transfer, the average Nusselt number value is much lower than the value seen for free convection but higher than forced convection. At lower Weissenberg numbers, it exhibits a plateau, which gradually decreases as the Weissenberg number increases. Ultimately, it again shows an almost plateau at higher values of the Weissenberg number. This heat transfer reduction (HTR) with the Weissenberg number for viscoelastic fluids in the mixed convection case happens despite the presence of elastic instability and turbulence inside the present geometry, as evident in Figs. 8 and 7. In general, elastic turbulence tends to increase the rates of transport processes such as mixing or heat transfer [42]. However, in the present case, the heat transfer rate decreases. The main reason behind this is that the thermal boundary layer thickness increases with the Weissenberg number, as can be seen from Fig. 10. This causes an increasing resistance to the heat transfer rate with the increasing value of the Weissenberg number. Furthermore, although the velocity fluctuation is present at higher Weissenberg numbers, it does not cause a strong bulk motion, which could facilitate the mixing of hot and cold fluids within the present geometry and eventually could increase the heat transfer rate. It was also noticeable in the plots of streamlines, where they were seen to be less distorted and more organized with the increasing value of the Weissenberg number (Fig. 6). The velocity magnitude value also hardly increased with the Weissenberg number despite the presence of elastic instability and elastic turbulence. The intensity of velocity fluctuation was seen to be mostly dominated near the inner rotating cylinder within the thermal boundary layers (Fig. 7). However, it does not facilitate reducing the thickness of the thermal boundary layers. The HTR with the Weissenberg number in viscoelastic fluids was also observed in other experimental and numerical studies like the Rayleigh-Bénard convection in a cavity [45,46]. In particular, these studies observed a deterioration and then an enhancement in the heat transfer rate with the increasing value of the Weissenberg number. In contrast, we have observed only its deterioration within the present range of the Weissenberg number considered in this study. The flow dynamics and heat transfer aspects, particularly this deterioration in the heat transfer rate with the

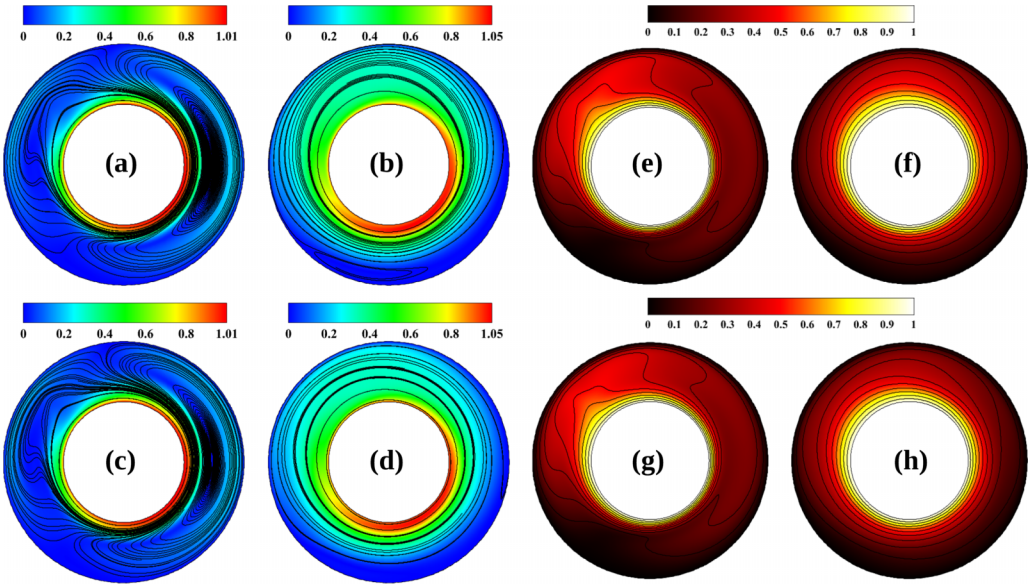

FIG. 12. Time-averaged streamlines and velocity magnitude plots at Weissenberg numbers 5 [(a) plane 1 and (c) plane 2] and 20 [(b) plane 1 and (d) plane 2]. The corresponding time-averaged temperature and isotherm distributions at Weissenberg numbers 5 [(e) plane 1 and (g) plane 2] and 20 [(f) plane 1 and (h) plane 2].

Weissenberg number in the case of mixed convection, are further illustrated with the help of the viscoelastic kinetic energy budget analysis presented in the subsequent section.

D. Limited three-dimensional simulations

In this study, we have further conducted three-dimensional (3D) simulations at two different Weissenberg number values, namely, 5 and 20. These 3D simulations are focused on mixed convection heat transfer only, where viscoelastic fluids exhibit maximum unsteadiness. The purpose of these 3D simulations is to compare flow dynamics and heat transfer rates with corresponding two-dimensional (2D) simulations. The present 3D geometry is constructed with a thickness of σ in the x_3 direction, consistent with the difference between the outer and inner cylinder radii. We have applied periodic boundary conditions to all variables perpendicular to the x_3 direction, which was also used in several prior studies [59,60]. Boundary conditions for the remaining planes remain the same as those used in 2D simulations. The present 3D simulations used a total of 3 024 000 cells, and only some limited 3D simulations were carried out with these cell numbers. This is because the computational hours (CPUh) increased drastically due to the increase in the total number of cells in the case of 3D simulations compared to 2D simulations. For instance, at Wi $= 20$, CPUh for 2D simulations was up to 3000, whereas the corresponding CPUh for 3D simulations was up to 75 000 to reach the statistically stationary state. Therefore, an increment of up to 25-fold was seen in the computational hours in the case of 3D simulations compared to 2D simulations.

We have presented time-averaged streamlines and velocity magnitude plots, along with temperature distribution and isotherms, at planes normal to the x_3 direction, specifically one plane at $x_3 = 0$ (plane 1) and the other at $x_3 = \sigma/2$ (plane 2) in Fig. 12. A careful observation reveals that the patterns in both streamline and isotherm profiles follow almost the same trend along these planes. These patterns also qualitatively match with those obtained from 2D simulations. Furthermore, not only was a qualitative match observed in the time-averaged fluid flow and heat transfer visualizations, but it was also obtained in the surface-averaged quantities. For instance,

the surface-averaged Nusselt number values are 2.196 and 1.584 at Wi = 5 and 20, respectively, in the case of 2D simulations. The corresponding values in the case of 3D simulations are 2.194 and 1.551. It can be seen that the Nusselt number values decrease with the Weissenberg number in 3D simulations, as also observed in 2D simulations. Moreover, the percentage difference between Nusselt number values obtained from 3D and 2D simulations remains below 1 for both Weissenberg number values. Therefore, these results suggest that, within the parameters examined in this study, flow dynamics and heat transfer phenomena in the present geometry are not significantly influenced by spatial dimensionality.

E. Viscoelastic kinetic energy budget analysis

Based on the analysis of Zheng *et al.* [61] and Cheng *et al.* [45], we have performed the viscoelastic kinetic energy budget analysis to gain more insights into the fluctuating and time-dependent flow and heat transfer phenomena seen in the mixed convection heat transfer. This analysis will facilitate a better understanding of the underlying physics considering the different components of fluid field energy, which denote the global and local kinetic energy exchanges, as shown in the following equation:

$$\frac{dE_{ij}}{dt} = \chi_{P,ij} + \chi_{D,ij} + \chi_{V,ij} + \chi_{G,ij} + \chi_{F,ij}. \tag{13}$$

In the above equation, $E_{ij} = \frac{1}{2}\langle u_i\rangle\langle u_j\rangle\delta_{ij}$ is the kinetic energy, $\chi_{P,ij} = -\langle u_i\rangle\langle u_j\rangle\frac{\partial\langle u_i\rangle}{\partial x_j}$ accounts for the inertial energy production, $\chi_{D,ij} = -\frac{\partial(\langle p\rangle\langle u_i\rangle)}{\partial x_j}\delta_{ij} + \frac{\beta}{\mathrm{Re}}\frac{\partial^2 E_{ij}}{\partial x_j^2}$ signifies the energy transport due to pressure diffusion and molecular viscous transport, $\chi_{V,ij} = -\frac{\beta}{\mathrm{Re}}\frac{\partial\langle u_i\rangle}{\partial x_j}\frac{\partial\langle u_i\rangle}{\partial x_j}$ represents the viscous dissipation term, $\chi_{G,ij} = (\frac{1-\beta}{\mathrm{Re}})(\frac{\partial(\langle u_i\rangle\langle\tau_{ij}\rangle)}{\partial x_j} - \langle\tau_{ij}\rangle\frac{\partial\langle u_i\rangle}{\partial x_j})$ denotes the energy transition between the flow structure and polymer molecules due to their stretching and relaxation mechanisms, and $\chi_{F,ij} = \frac{\mathrm{Gr}}{\mathrm{Re}^2}\langle\phi\rangle\langle u_i\rangle\delta_{i2}$ represents the buoyancy flux input. Here, δ_{ij} is the Kronecker delta function, and the $\langle\cdot\rangle$ operator denotes the time-averaged value of a variable. Furthermore, a spatial average over the whole computational domain was also performed for each component as follows: $E = \frac{1}{S}\iint E_{ij}\,dx_1dx_2$, $\chi_P = \frac{1}{S}\iint \chi_{P,ij}\,dx_1dx_2$, $\chi_D = \frac{1}{S}\iint \chi_{D,ij}\,dx_1dx_2$, $\chi_V = \frac{1}{S}\iint \chi_{V,ij}\,dx_1dx_2$, $\chi_G = \frac{1}{S}\iint \chi_{G,ij}\,dx_1dx_2$, and $\chi_F = \frac{1}{S}\iint \chi_{F,ij}\,dx_1dx_2$, where S is the surface area of the whole computational domain.

In Figs. 13(a)–13(c), we illustrate the inertial energy production in viscoelastic fluids with varying Weissenberg numbers, including the case of a Newtonian fluid for which the Weissenberg number is zero. Irrespective of the fluid type, whether Newtonian or viscoelastic, we observe consistently high inertial energy production near the inner cylinder. This is attributed to the substantial impact of inner cylinder rotation in this region. As the Weissenberg number increases, the width as well as the magnitude of the high-χ_P region increases, and the positions of the highest (positive) and lowest (negative) regions of inertial energy production change significantly. For Newtonian fluids, the highest region is present between $\theta = 90^\circ$ and 180°, whereas the lowest region is present between $\theta = 270^\circ$ and 0°. However, these regions gradually shift their positions by rotating clockwise for viscoelastic fluids with increasing values of the Weissenberg number. This observation suggests that the flow field undergoes substantial changes as the Weissenberg number gradually increases, subsequently exerting a significant influence on the heat transfer rate.

Figures 13(d)–13(f) present the spatial distribution of energy transport arising from pressure diffusion and molecular viscous transport. In the case of Newtonian fluids [Fig. 13(d)] and viscoelastic fluids with low Weissenberg numbers, the dominant mechanism for energy transport is molecular viscous transport, particularly near the surface of the inner rotating cylinder. However, as the Weissenberg number gradually increases to higher values, the energy transport due to pressure diffusion surpasses that of molecular viscous transport. This shift is anticipated, given that fluid viscoelasticity leads to an increased pressure gradient [62,63], consequently enhancing the

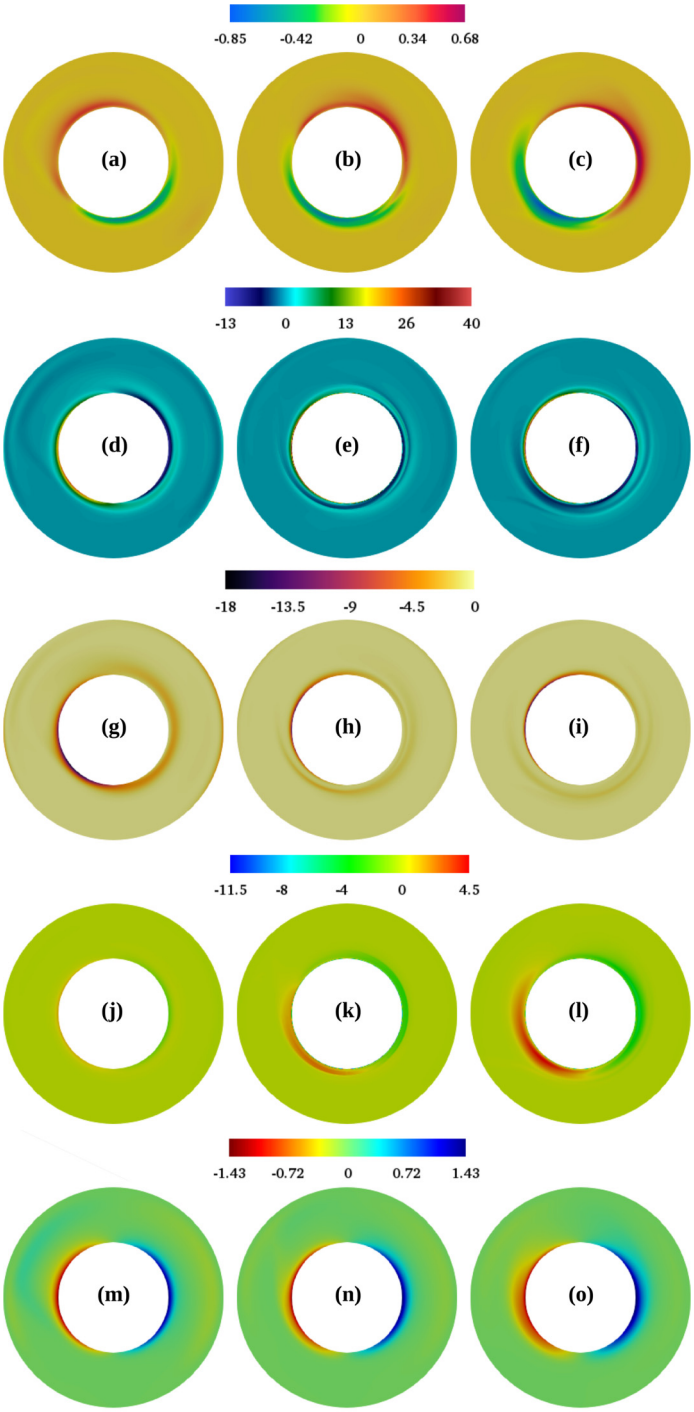

FIG. 13. Spatial variation of time-averaged terms appearing in the viscoelastic kinetic budget analysis [Eq. (13)] with Weissenberg number at $\mathrm{Ra} = 10^5$ and $\mathrm{Ri} = 1.429$. The combinations shown here are for (a) $\chi_{P,ij}$, $\mathrm{Wi} = 0$; (b) $\chi_{P,ij}$, $\mathrm{Wi} = 5$; (c) $\chi_{P,ij}$, $\mathrm{Wi} = 20$; (d) $\chi_{D,ij}$, $\mathrm{Wi} = 0$; (e) $\chi_{D,ij}$, $\mathrm{Wi} = 5$; (f) $\chi_{D,ij}$, $\mathrm{Wi} = 20$; (g) $\chi_{V,ij}$, $\mathrm{Wi} = 0$; (h) $\chi_{V,ij}$, $\mathrm{Wi} = 5$; (i) $\chi_{V,ij}$, $\mathrm{Wi} = 20$; (j) $\chi_{G,ij}$, $\mathrm{Wi} = 0.01$; (k) $\chi_{G,ij}$, $\mathrm{Wi} = 5$; (l) $\chi_{G,ij}$, $\mathrm{Wi} = 20$; (m) $\chi_{F,ij}$, $\mathrm{Wi} = 0$; (n) $\chi_{F,ij}$, $\mathrm{Wi} = 5$; and (o) $\chi_{F,ij}$, $\mathrm{Wi} = 20$.

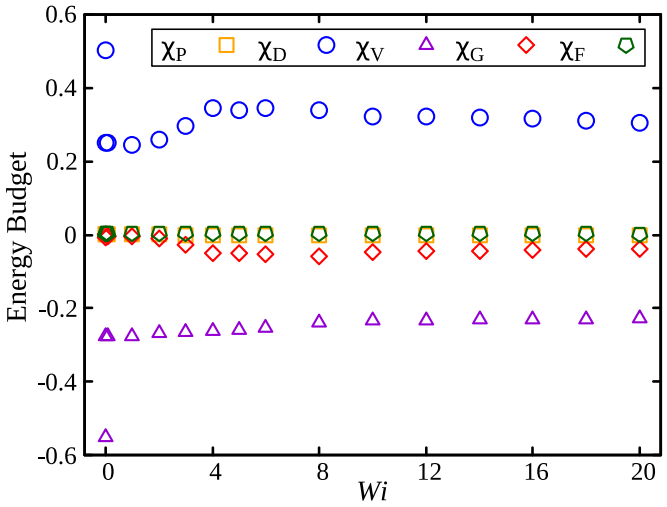

FIG. 14. Variation of different terms (spatiotemporally averaged) appearing in the viscoelastic kinetic energy budget analysis with Weissenberg number for Ra $= 10^5$ and Ri $= 1.429$.

contribution of pressure diffusion to energy transport. Similar to the trend observed in inertial energy production, the region characterized by high χ_D also contracts as the Weissenberg number increases. Figures 13(g)–13(i) illustrate the spatial distribution of viscoelastic kinetic energy transfer attributed to viscous dissipation for different Weissenberg number values. Irrespective of the fluid type, this energy transfer remains close to zero except in the vicinity of the inner rotating cylinder, where intense shearing between fluid layers occurs. Notably, this transfer is more pronounced in the case of Newtonian fluids [Fig. 13(g)], and it is decreased as the Weissenberg number gradually increases. Figures 13(j)–13(l) present the spatial variation of energy exchange between flow structures and polymer molecules. When this term is positive, it acts as an energy source in the system, while it functions as an energy sink when negative [45]. For viscoelastic fluids with a very low Weissenberg number of 0.01, this term remains almost zero due to the presence of very low values of elastic stresses. However, its magnitude increases as the Weissenberg number increases, particularly near the inner cylinder, where higher elastic stresses are generated due to cylinder rotation. Specifically, energy is transferred from the flow structure to the polymer molecules in the region between $\theta = 270^\circ$ and 0°, while the energy flows from the polymers to the flow field in the region between $\theta = 180^\circ$ and 270°. On the other hand, Figs. 13(m)–13(o) demonstrate the spatial variation of kinetic energy transfer due to buoyant flux. This transfer is prominent along the two vertical sides of the inner cylinder, and its width increases as the Weissenberg number increases.

The spatial variations of different components of kinetic energy transfer are depicted in time-averaged surface plots, providing insights into their distribution. However, for a comprehensive analysis of heat transfer aspects, it is crucial to calculate and understand the surface-averaged values. Thus, in Fig. 14, we present the variations of various components of the kinetic energy budget with respect to the Weissenberg number. The surface-averaged value of inertial energy production (χ_P) remains consistently low, near zero, and largely independent of the Weissenberg number. In contrast, energy transfer attributed to pressure diffusion and molecular viscous transport (χ_D) exhibits variations. It is highest for Newtonian fluids and gradually decreases for viscoelastic fluids as the Weissenberg number increases up to around 5. Beyond this point, it remains relatively constant. As mentioned earlier, for Newtonian and low-Weissenberg-number viscoelastic fluids, energy transfer due to viscous molecular transport (which contributes positively) dominates. However, as the Weissenberg number increases, energy transport due to pressure diffusion (with a negative contribution) becomes dominant, reducing the overall energy contribution. The energy transfer (χ_V)

attributed to viscous dissipation (which results in energy loss) is highest in magnitude for Newtonian fluids due to the sole presence of solvent molecules, promoting shearing among them. In viscoelastic fluids, introducing polymer molecules reduces the solvent's concentration, leading to a decrease in the viscous dissipation associated with shearing among solvent fluid layers. This magnitude remains almost constant irrespective of the value of the Weissenberg number. The buoyancy flux input (χ_F) remains consistently small, close to zero, and independent of the Weissenberg number. Conversely, the surface-averaged value of energy exchange between fluid structure and polymer molecules (χ_G) remains negative and increases in magnitude with increasing Weissenberg number up to a Weissenberg number of around 8, and then it starts to decrease gradually on further increasing the Weissenberg number value. This observation suggests that when polymer molecules stretch in the flow field, energy transfers from fluid structure to polymer molecules, decreasing the overall kinetic energy within the system. As discussed in the preceding section, it eventually inhibits the bulk motion inside the system and leads to a decrease in the heat transfer rate. However, at higher Weissenberg number values, the negative contribution of (χ_G) to the overall kinetic energy starts to decrease, suggesting a decrease in the energy transfer from fluid structure to polymer molecules. This is due to the increase in the intensity of elastic turbulence at higher Weissenberg numbers, where energy transfer starts to happen from polymer molecules to fluid structures. As a result, the heat transfer rate does not decrease to that extent, but instead, it remains almost constant at higher Weissenberg numbers (Fig. 11). Our observation and explanation are in line with that seen and provided by Cheng *et al.* [45] during the Rayleigh-Bénard convection of viscoelastic fluids in a cavity where they also observed such nonmonotonic dependence of the Weissenberg number on χ_G.

V. CONCLUSIONS

This study conducted an extensive numerical investigation to explore forced, free, and mixed convection heat transfer phenomena in viscoelastic fluids confined between two concentric cylinders, with the inner cylinder undergoing rotation. The rheological behavior of the viscoelastic fluid was represented using the Oldroyd-B constitutive equation, and the numerical simulations were executed using the open-source code OPENFOAM to solve the governing equations. As the viscoelasticity of the fluid, quantified by the Weissenberg number, increased, a transition in the flow behavior was observed in the cases of free and mixed convection conditions. In particular, the flow field shifted from a steady state to unsteady periodic, quasiperiodic, and ultimately aperiodic or chaotic states. This transition was attributed to the emergence of elastic instability and ensuing elastic turbulence within the flow field as fluid viscoelasticity increased. On the other hand, the heat transfer rate was almost independent of the Weissenberg number in the case of forced convection, whereas it slightly increased in the case of free convection. However, in the case of mixed convection, the heat transfer rate first demonstrated a gradual decrease with the Weissenberg number, which remained almost constant at higher Weissenberg numbers. The viscoelastic kinetic energy budget was comprehensively analyzed to elucidate this heat transfer deterioration. The investigation revealed a notable phenomenon wherein energy transition occurred from flow structure to polymer molecules within viscoelastic fluids. This energy transfer intensified with the Weissenberg number, consequently decreasing the system's kinetic energy and, subsequently, the heat transfer rate. However, at higher Weissenberg numbers, this energy transition decreased due to the increased intensity of elastic turbulence, and subsequently, the heat transfer rate remained almost constant instead of decreasing steadily.

ACKNOWLEDGMENTS

We acknowledge M. Kumar for constructing the computational domain and the National Supercomputing Mission (NSM) for providing computing resources of "PARAM Smriti" at NABI, Mohali (accessed by C.S.) and "PARAM Himalaya" at IIT Mandi (accessed by A.C.), which are

implemented by C-DAC and supported by the Ministry of Electronics and Information Technology (MeitY) and Department of Science and Technology (DST), Government of India. A.C. would also like to thank the Ministry of Education, Government of India, for the financial support provided by the PMRF (Cycle-9).

APPENDIX: GOVERNING EQUATIONS FOR PURELY FREE CONVECTION

We nondimensionalize all the governing equations [Eqs. (1)–(6)] using the following scaling variables in the case of purely free convection:

$$x_i = \frac{x_i^*}{\sigma} g, \quad u_i = \frac{u_i^*}{\sqrt{\sigma g \beta_T \Delta T}}, \quad t = t^* \sqrt{\frac{g\beta_T \Delta T}{\sigma}},$$

$$p = \frac{p^*}{\rho_{\text{ref}} \sigma g \beta_T \Delta T}, \quad \tau_{ij}^p = \frac{\tau_{ij}^{p*}}{\eta_p} \sqrt{\frac{\sigma}{g\beta_T \Delta T}}, \quad \text{and} \quad \phi = \frac{T - T_C}{T_H - T_C}$$

The nondimensional forms of the governing equations are obtained as follows:
The continuity equation is

$$\frac{\partial u_i}{\partial x_i} = 0, \tag{A1}$$

the momentum equation is

$$\frac{\partial u_i}{\partial t} + u_j \frac{\partial u_i}{\partial x_j} = -\frac{\partial p}{\partial x_i} + \frac{\beta}{\sqrt{\text{Ra/Pr}}} \frac{\partial}{\partial x_j}\left(\frac{\partial u_i}{\partial x_j}\right) + \frac{1-\beta}{\sqrt{\text{Ra/Pr}}} \frac{\partial \tau_{ij}^p}{\partial x_j} + \phi \delta_{i2}, \tag{A2}$$

the energy equation is

$$\frac{\partial \phi}{\partial t} + u_j \frac{\partial \phi}{\partial x_j} = \frac{1}{\sqrt{\text{Ra Pr}}} \frac{\partial}{\partial x_j}\left(\frac{\partial \phi}{\partial x_j}\right), \tag{A3}$$

and the polymeric conformation tensor transport equation is

$$\frac{\partial C_{ij}}{\partial t} + u_k \frac{\partial C_{ij}}{\partial x_k} - \frac{\partial u_i}{\partial x_k} C_{kj} - \frac{\partial u_j}{\partial x_k} C_{ik} = \frac{\delta_{ij} - C_{ij}}{\text{Wi}}. \tag{A4}$$

In the above equations, $\text{Ra} = \frac{C_p \rho^2 g \beta_T (T_H - T_C) \sigma^3}{\eta_0 k}$ is the Rayleigh number, $\text{Pr} = \frac{C_p \eta_0}{k}$ is the Prandtl number, $\text{Wi} = \lambda \sqrt{\frac{g\beta_T \Delta T}{\sigma}}$ is the Weissenberg number, and $\beta = \frac{\eta_s}{\eta_0} = \frac{\eta_s}{\eta_s + \eta_p}$ is the polymer viscosity ratio, which is defined as the ratio of the solvent to that of the zero-shear rate viscosity of the polymer solution.

[1] C. Gazley, Jr., Heat-transfer characteristics of the rotational and axial flow between concentric cylinders, Trans. Am. Soc. Mech. Eng. **80**, 79 (1958).
[2] I. S. Bjorklund and W. M. Kays, Heat transfer between concentric rotating cylinders, J. Heat Transfer **81**, 175 (1959).
[3] G. I. Taylor, Stability of a viscous liquid contained between two rotating cylinders, Philos. Trans. R. Soc. London A **223**, 289 (1923).
[4] R. C. Di Prima and H. L. Swinney, Instabilities and transition in flow between concentric rotating cylinders, in *Hydrodynamic Instabilities and the Transition to Turbulence*, Topics in Applied Physics Vol. 45 (Springer, Berlin, 1981), pp. 139–180.
[5] D. Coles, Transition in circular Couette flow, J. Fluid Mech. **21**, 385 (1965).

[6] M. Fénot, Y. Bertin, E. Dorignac, and G. Lalizel, A review of heat transfer between concentric rotating cylinders with or without axial flow, Int. J. Therm. Sci. **50**, 1138 (2011).
[7] T. H. Kuehn and R. J. Goldstein, An experimental and theoretical study of natural convection in the annulus between horizontal concentric cylinders, J. Fluid Mech. **74**, 695 (1976).
[8] R. Kumar, Study of natural convection in horizontal annuli, Int. J. Heat Mass Transfer **31**, 1137 (1988).
[9] J.-S. Yoo, Prandtl number effect on bifurcation and dual solutions in natural convection in a horizontal annulus, Int. J. Heat Mass Transfer **42**, 3279 (1999).
[10] C. P. Desai and K. Vafai, An investigation and comparative analysis of two- and three-dimensional turbulent natural convection in a horizontal annulus, Int. J. Heat Mass Transfer **37**, 2475 (1994).
[11] K. Khanafer and A. J. Chamkha, Mixed convection within a porous heat generating horizontal annulus, Int. J. Heat Mass Transfer **46**, 1725 (2003).
[12] S. A. Nada and M. A. Said, Effects of fins geometries, arrangements, dimensions and numbers on natural convection heat transfer characteristics in finned-horizontal annulus, Int. J. Thermal Sci. **137**, 121 (2019).
[13] R. E. Powe, C. T. Carley, and E. H. Bishop, Free convective flow patterns in cylindrical annuli, J. Heat Transfer **91**, 310 (1969).
[14] H. K. Dawood, H. A. Mohammed, N. A. Che Sidik, K. M. Munisamy, and M. A. Wahid, Forced, natural and mixed-convection heat transfer and fluid flow in annulus: A review, Int. Commun. Heat Mass Transfer **62**, 45 (2015).
[15] H. Aoki, H. Nohira, and H. Arai, Convective heat transfer in an annulus with an inner rotating cylinder, Bull. JSME **10**, 523 (1967).
[16] T. S. Lee, Numerical experiments with laminar fluid convection between concentric and eccentric heated rotating cylinders, Numer. Heat Transfer **7**, 77 (1984).
[17] T. S. Lee, Laminar fluid convection between concentric and eccentric heated horizontal rotating cylinders for low-Prandtl-number fluids, Int. J. Numer. Methods Fluids **14**, 1037 (1992).
[18] S. R. M. Gardiner and R. H. Sabersky, Heat transfer in an annular gap, Int. J. Heat Mass Transfer **21**, 1459 (1978).
[19] P. R. N. Childs and C. A. Long, A review of forced convective heat transfer in stationary and rotating annuli, Proc. Ins. Mech. Eng. Part C: J. Mech. Eng. Sci. **210**, 123 (1996).
[20] T. Fusegi, B. Farouk, and K. S. Ball, Mixed-convection flows within a horizontal concentric annulus with a heated rotating inner cylinder, Numer. Heat Transfer **9**, 591 (1986).
[21] J.-S. Yoo, Mixed-convection of air between two horizontal concentric cylinders with a cooled rotating outer cylinder, Int. J. Heat Mass Transfer **41**, 293 (1998).
[22] L. Yang and B. Farouk, Three-dimensional mixed convection flows in a horizontal annulus with a heated rotating inner circular cylinder, Int. J. Heat Mass Transfer **35**, 1947 (1992).
[23] K. Kahveci, Stability of unsteady mixed convection in a horizontal concentric annulus, J. Appl. Fluid Mech. **9**, 2141 (2016).
[24] R. P. Chhabra and J. F. Richardson, *Non-Newtonian Flow and Applied Rheology: Engineering Applications* (Butterworth-Heinemann, London, 2011).
[25] F. A. Morrison, *Understanding Rheology* (Oxford University Press, New York, 2001), Vol. 1.
[26] N. Phan-Thien and N. Mai-Duy, *Understanding Viscoelasticity: An Introduction to Rheology* (Springer, Berlin, 2013).
[27] R. Keunings, On the high Weissenberg number problem, J. Non-Newtonian Fluid Mech. **20**, 209 (1986).
[28] R. Fattal and R. Kupferman, Constitutive laws for the matrix-logarithm of the conformation tensor, J. Non-Newtonian Fluid Mech. **123**, 281 (2004).
[29] R. G. Larson, E. S. G. Shaqfeh, and S. J. Muller, A purely elastic instability in Taylor-Couette flow, J. Fluid Mech. **218**, 573 (1990).
[30] P. Pakdel and G. H. McKinley, Elastic instability and curved streamlines, Phys. Rev. Lett. **77**, 2459 (1996).
[31] V. Steinberg, Elastic turbulence: An experimental view on inertialess random flow, Annu. Rev. Fluid Mech. **53**, 27 (2021).
[32] A. Groisman and V. Steinberg, Elastic turbulence in a polymer solution flow, Nature (London) **405**, 53 (2000).

[33] A. Groisman and V. Steinberg, Elastic turbulence in curvilinear flows of polymer solution, New J. Phys. **6**, 29 (2004).
[34] R. D. Whalley, W. M. Abed, D. J. C. Dennis, and R. J. Poole, Enhancing heat transfer at the micro-scale using elastic turbulence, Theor. Appl. Mech. Lett. **5**, 103 (2015).
[35] D.-Y. Li, H. Zhang, J.-P. Cheng, X.-B. Li, F.-C. Li, S. Qian, and S. W. Joo, Numerical simulation of heat transfer enhancement by elastic turbulence in a curvy microchannel, Microfluid. Nanofluid. **21**, 25 (2017).
[36] B. Traore, C. Castelain, and T. Burghelea, Efficient heat transfer in a regime of elastic turbulence, J. Non-Newtonian Fluid Mech. **223**, 62 (2015).
[37] G. Yao, H. Yang, J. Zhao, and D. Wen, Experimental study on flow and heat transfer enhancement by elastic instability in swirling flow, Int. J. Therm. Sci. **157**, 106504 (2020).
[38] R. J. Poole, B. Budhiraja, A. R. Cain, and P. A. Scott, Emulsification using elastic turbulence, J. Non-Newtonian Fluid Mech. **177-178**, 15 (2012).
[39] T. Burghelea, E. Segre, and V. Steinberg, Mixing by polymers: Experimental test of decay regime of mixing, Phys. Rev. Lett. **92**, 164501 (2004).
[40] A. Groisman and V. Steinberg, Efficient mixing at low Reynolds numbers using polymer additives, Nature (London) **410**, 905 (2001).
[41] M. Grilli, A. Vázquez-Quesada, and M. Ellero, Transition to turbulence and mixing in a viscoelastic fluid flowing inside a channel with a periodic array of cylindrical obstacles, Phys. Rev. Lett. **110**, 174501 (2013).
[42] C. Sasmal, Applications of elastic instability and elastic turbulence: Review, limitations, and future directions, arXiv:2301.02395.
[43] S. Gupta, A. Chauhan, and C. Sasmal, Influence of elastic instability and elastic turbulence on mixed convection of viscoelastic fluids in a lid-driven cavity, Int. J. Heat Mass Transfer **186**, 122469 (2022).
[44] S. Gupta and C. Sasmal, Effect of cavity aspect ratio on mixed convective heat transfer phenomenon inside a lid-driven cavity due to elastic turbulence, Phys. Fluids **35**, 033114 (2023).
[45] J.-P. Cheng, H.-N. Zhang, W.-H. Cai, S.-N. Li, and F.-C. Li, Effect of polymer additives on heat transport and large-scale circulation in turbulent Rayleigh-Bénard convection, Phys. Rev. E **96**, 013111 (2017).
[46] P. Wei, R. Ni, and K.-Q. Xia, Enhanced and reduced heat transport in turbulent thermal convection with polymer additives, Phys. Rev. E **86**, 016325 (2012).
[47] H. Demir, Rayleigh–Benard convection of viscoelastic fluid, Appl. Math. Comput. **136**, 251 (2003).
[48] W. Cai, T. Wei, X. Tang, Y. Liu, B. Li, and F. Li, The polymer effect on turbulent Rayleigh-Bénard convection based on PIV experiments, Exp. Thermal Fluid Sci. **103**, 214 (2019).
[49] https://www.openfoam.org.
[50] F. Pimenta and M. Alves, fppimenta/rheoTool, https://github.com/fppimenta/rheoTool (2016).
[51] A. Bejan, *Convection Heat Transfer* (John Wiley & Sons, New York, 2013).
[52] R. B. Bird, C. F. Curtiss, R. C. Armstrong, and O. Hassager, *Dynamics of Polymeric Liquids, Volume 2: Kinetic Theory* (Wiley-Interscience, New York, 1987).
[53] D. F. James, Boger fluids, Annu. Rev. Fluid Mech. **41**, 129 (2009).
[54] M. A. Alves, P. J. Oliveira, and F. T. Pinho, A convergent and universally bounded interpolation scheme for the treatment of advection, Int. J. Numer. Methods Fluids **41**, 47 (2003).
[55] M. A. Ajiz and A. Jennings, A robust incomplete choleski-conjugate gradient algorithm, Int. J. Numer. Methods Eng. **20**, 949 (1984).
[56] J. Lee, J. Zhang, and C. C. Lu, Incomplete LU preconditioning for large scale dense complex linear systems from electromagnetic wave scattering problems, J. Comput. Phys. **185**, 158 (2003).
[57] R. Fattal and R. Kupferman, Time-dependent simulation of viscoelastic flows at high Weissenberg number using the log-conformation representation, J. Non-Newtonian Fluid Mech. **126**, 23 (2005).
[58] F. Pimenta and M. A. Alves, Stabilization of an open-source finite-volume solver for viscoelastic fluid flows, J. Non-Newtonian Fluid Mech. **239**, 85 (2017).
[59] S. Y. Jung and H. J. Sung, Characterization of the three-dimensional turbulent boundary layer in a concentric annulus with a rotating inner cylinder, Phys. Fluids **18**, 115102 (2006).

[60] F. Lin, J. Song, N. Liu, Z. Wan, X.-Y. Lu, and B. Khomami, Maximum drag enhancement asymptote in turbulent Taylor–Couette flow of dilute polymeric solutions, J. Non-Newtonian Fluid Mech. **323**, 105172 (2024).

[61] X. Zheng, M. Boutaous, S. Xin, D. A. Siginer, and W. Cai, Time-dependent oscillating viscoelastic Rayleigh-Bénard convection: Viscoelastic kinetic energy budget analysis, Phys. Rev. Fluids **8**, 023303 (2023).

[62] D. F. James and A. Tripathi, Pressure drop in a converging channel with viscoelastic polymer solutions having power-law viscous behaviour, J. Non-Newtonian Fluid Mech. **312**, 104974 (2023).

[63] H. Bendová, B. Šiška, and I. Machač, Pressure drop excess in the flow of viscoelastic liquids through fixed beds of particles, Chem. Eng. Proc.: Process Intensification **48**, 29 (2009).